

Rapid and Accurate Measurement of Polarization and Fading of Weak VHF Signals Obliquely Reflected from Sporadic-E Layers

Chris J. Deacon, Ben A. Witvliet, *Senior Member, IEEE*, Simon N. Steendam, and Cathryn N. Mitchell

Abstract— In the E-region of the ionosphere, at heights between 90 and 130 km, thin patches of enhanced ionization occur intermittently. The electron density in these sporadic-E (Es) clouds can sometimes be so high that radio waves with frequencies up to 150 MHz are obliquely reflected. While this phenomenon is well known, the reflection mechanism itself is not well understood. To investigate this question, an experimental system has been developed for accurate polarimetric and fading measurements of 50 MHz radio waves obliquely reflected by mid-latitude Es layers. The overall sensitivity of the system is optimized by reducing environmental electromagnetic noise, giving the ability to observe weak, short-lived 50 MHz Es propagation events. The effect of the ground reflection on observed polarization is analyzed and the induced amplitude and phase biases are compensated for. It is found that accurate measurements are only possible below the pseudo-Brewster angle. To demonstrate the effectiveness of the system, initial empirical results are presented which provide clear evidence of magneto-ionic double refraction.

Index Terms—VHF, ionosphere, radio wave propagation, sporadic-E, polarization, radio noise, Brewster angle

I. INTRODUCTION

The ionosphere is a region of partially ionized plasma, embedded in the neutral atmosphere at heights from around 60 km to over 1000 km. The plasma is mainly generated by photoionization of gas molecules and atoms by solar radiation. Reflection of HF radio waves from the F-region ionosphere is established as being through the mechanism of magneto-ionic double refraction [1], [2], which regularly enables long-distance propagation of radio signals at frequencies up to 30 MHz. Mid-latitude sporadic-E clouds (commonly abbreviated as ‘Es’) are a transient feature consisting of thin layers of dense but patchy ionization which occur in the lower ionosphere [3]–[5]. The process of formation is different from that of the rest of the ionosphere and it can produce much higher electron densities, sometimes permitting oblique reflection of radio waves up to 150 MHz [6], see Fig. 1. The presence of Es clouds is difficult to predict and therefore the International Telecommunication Union’s recommended approach to estimating the likelihood of occurrence and strength of signals reflected from Es layers is purely statistically based [7].

Despite its unpredictable and intermittent nature, the impact of reflections from Es layers on communications services can be significant. In the high frequency (HF) range, 3–30 MHz, the presence of Es layers can dramatically shorten the ionospheric reflection distance, eliminating the signal from the desired station and/or causing

interference from stations at shorter distances and introducing multipath fading [8, pp. 184–186]. In the very high frequency (VHF) range between 30 and 150 MHz, Es layers can intermittently support long-distance communication [6] but such effects are not predictable and are often brief, so VHF radio services are either designed for line-of-sight distances or they adopt alternative techniques such as troposcatter. At times, such services can be vulnerable to interference from very strong unwanted signals arriving via Es reflections [9].

The impact of Es effects on trans-ionospheric communications, at much higher frequencies, can also be significant. Es layers exhibit very sharp ionization density gradients. These frequently introduce significant amplitude and phase disturbance effects into trans-ionospheric transmissions from global navigation satellites, potentially causing positioning errors or even complete loss of signals, particularly for paths entering the ionosphere tangentially [10].

The mechanism for the oblique reflection of radio waves from Es layers is not well understood, with candidates including specular reflection [11], [12], scattering [11], and magneto-ionic double refraction [13]. Magneto-ionic splitting can be observed in vertical soundings from Es layers using ionosondes [14], but it has not been conclusively demonstrated for oblique reflection at frequencies above 30 MHz. The purpose of the current research is therefore to gain insight into whether Es-layer propagation at 50 MHz exhibits the characteristics of specular reflection, magneto-ionic double refraction, scattering, or some combination of all three. The polarization and fading characteristics of radio waves reflected from Es layers are proposed as a marker for the presence of magneto-ionic effects.

This research requires fast and accurate field strength and polarization measurements. This is particularly challenging due to the influence of the ground reflection. Furthermore, as measurement of the weaker signals around the onset and termination of the Es-propagation interval is essential for the understanding of the phenomenon, sensitivity is important and ambient electromagnetic noise (‘radio noise’) must be minimized.

This article will focus on the design of the experiment, and the design and calibration of the polarimetric system. To demonstrate system performance, initial results will be presented.

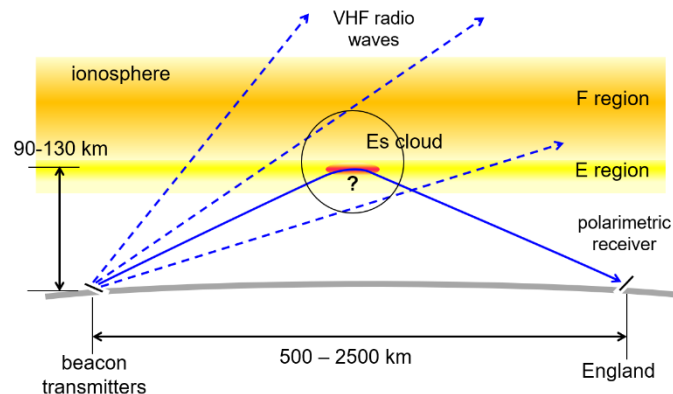


Fig. 1. Reflection of VHF radio waves by sporadic-E (Es) clouds.

Manuscript received xxxxxx.

Chris Deacon and Cathryn Mitchell are with the University of Bath, Dept. of Electronic & Electrical Engineering, Centre for Space, Atmospheric and Oceanic Science, Claverton Down, Bath, BA2 7AY, United Kingdom (e-mail: c.j.deacon@bath.ac.uk; c.n.mitchell@bath.ac.uk).

Ben Witvliet is with the University of Twente, Faculty of EEMCS, Radio Systems group, P. O. Box 217, 7500AE Enschede, The Netherlands (e-mail: b.a.witvliet@utwente.nl).

Simon Steendam is with the Radiocommunications Agency Netherlands, Spectrum Management Dept., P. O. Box 450, 9700AL Groningen, The Netherlands (e-mail: simon.steendam@agentschaptelecom.nl).

Digital Object Identifier xxx/xxxx.xxx

The article is structured as follows: Section II provides an overview of the origin and characteristics of Es. The experiment and the design of the measurement system are described in Sections III and IV. In Sections V and VI, the influence of the ground reflection is analyzed, and related corrections are determined. Post-processing, calibration and measurement uncertainty estimation are described in Section VII. Section VIII presents initial results for two Es propagation paths, to demonstrate system performance, with conclusions in Section IX.

II. THE ORIGIN AND CHARACTERISTICS OF ES

Sporadic-E consists of thin layers of dense but patchy ionization which occur transiently in the E region of the ionosphere. It was first detected during early experiments with ionosondes in the 1930s [15], with oblique long-distance reflections being observed soon afterwards [16]. The current understanding of the origin and characteristics of Es is summarized in this section, but for more information see the extensive reviews published by Whitehead [3], Mathews [4] and Haldoupis [17] and references therein.

A. Formation of Es layers and clouds

There are three broad types of Es, occurring in different geographical zones and with different characteristics. Equatorial sporadic-E is driven by instabilities in ionospheric currents and occurs close to the magnetic equator. Auroral E is produced in the northern and southern auroral zones by the particle precipitation from the magnetosphere. Finally, Mid-latitude sporadic-E occurs in the northern and southern temperate zones [18] and is believed to be caused by wind shear. This article is concerned only with Mid-latitude sporadic-E (abbreviated as ‘Es’).

Es is made up of thin clouds or layers of enhanced ionization which occur at heights between 90 km and 130 km [17], [19], [20], with thickness between about 0.5 km and 5 km [21], [22] with horizontal extent from a few to hundreds of kilometers [23] and with significant internal structure [24], [25]. There is evidence for the existence of a number of ‘preferred heights’ for the layers to form at [26], [27] from which levels they are observed to descend at speeds of between 0.6 ms⁻¹ and 4 ms⁻¹ [21]. There is considerable variation in size and shape: sometimes layers can be large, flat and relatively uniform [28] but on other occasions they take the form of individual clouds of ionization with varying shapes and between 2 and 100 km in size, typically moving horizontally at 20 – 130 ms⁻¹ [3], [29]–[31].

The most detailed and complete picture of the global incidence of Es by season now comes from satellite radio occultation measurements [32]–[34]. Es is primarily a summer daytime phenomenon [32], [35] and in the Northern Hemisphere it exhibits a strong peak in the number and intensity of events between May and August each year [36]. A survey of observations of the diurnal and seasonal variation of the incidence of Es reflections [3, pp 410-11] indicates that a double-peaked pattern is frequently observed, particularly for the more intense Es events [37], with a maximum in mid-morning and another in the early evening.

The Windshear Theory, first proposed by Whitehead [38], is generally accepted as the explanation for the formation of Es. Metallic ions, mostly Mg⁺ and Fe⁺ arising from the disintegration of micrometeors as they burn up when entering the atmosphere [5], are swept together by geomagnetic Lorentz forces between opposing winds above and below, accumulating in the null between the two winds [17], [39]. The metal ions ‘drag’ their associated free electrons along with them so that overall charge neutrality is maintained. Metallic ions in the E layer have much longer lifetimes than gas ions because they are monatomic, making dielectric recombination a very slow process [40], [41]. This allows Es layers to persist. Diurnal and semi-diurnal tides, caused by solar heating, are known to be a major factor in the creation of wind-shear in the E region [4], [17] but it has

been suggested that other phenomena also have an influence, such as thunderstorms [42] and topographic features such as mountain ranges [43]. The relative importance of these factors is the subject of considerable debate [44].

B. Es radio wave propagation mechanisms

The mechanism for the oblique reflection of radio waves from Es layers is not well understood, with candidates including specular reflection [11], [12], [45], scattering [11], [12], and magneto-ionic double refraction [13]. Magneto-ionic double refraction in the ionosphere, whereby a wave launched vertically is split into two circularly polarized waves which travel at different speeds and therefore exhibit different time delays on reflection back to ground, was first observed in the 1930s [1]. The refractive index of an ionized plasma, from which the path of a wave can be derived by ray tracing, can be described by the Appleton-Hartree equation [2], [46], which describes the phase refractive index along the path of the wave in terms of the frequency of the wave and the parameters of the plasma:

$$n^2 = 1 - \frac{X}{1 - jZ - \left[\frac{Y_T^2}{2(1-X-jZ)} \right] \pm \sqrt{\frac{Y_T^2}{4(1-X-jZ)^2} + Y_L^2}} \quad (1)$$

where $X = \omega_N^2 / \omega^2$, $Y = \omega_B / \omega$, $Y_L = \omega_L / \omega$, $Y_T = \omega_T / \omega$, $Z = v / \omega$.

In (1), the refractive index n of the medium is derived from the angular frequency ω of the signal and from properties of the medium, where ω_N is the plasma frequency (the natural frequency of charge displacement), ω_B is the electron gyro frequency (the natural frequency at which the electrons rotate around the magnetic lines of force), ω_L and ω_T are the longitudinal and transverse components of ω_B relative to the direction of propagation, and v is the electron collision frequency. Y_L and Y_T are the magnetic terms and Z is the absorption term. It can be seen that the Appleton-Hartree equation generates two solutions for the refractive index because of the \pm term in the denominator. The two values correspond to two ‘characteristic waves’, which in general are elliptically polarized.

The polarization of each of the characteristic waves can be represented [2, pp 8-20] by the quantity R , the ratio of two orthogonal linear components of the field strength:

$$R = -\frac{j}{Y_L} \left(\left[\frac{Y_T^2}{2(1-X-jZ)} \right] \mp \sqrt{\frac{Y_T^2}{4(1-X-jZ)^2} + Y_L^2} \right) \quad (2)$$

where X , Y , Y_L , Y_T and Z have the same meanings as in (1).

The two solutions of (2) again correspond to the two characteristic waves. If R is a real quantity, the wave is linearly polarized and if R is complex, the wave is elliptically polarized. Only the characteristic waves can propagate unchanged in a plasma: the interaction of an incident linearly polarized wave with free electrons and the magnetic field in the ionosphere forces the incoming wave to decompose into ‘ordinary’ (O) and ‘extraordinary’ (X) elliptically polarized components with opposite senses of rotation. The characteristic waves travel at different velocities and can follow significantly different paths. The polarization of the downward wave exiting the ionosphere will normally be some combination of the O and X components, resulting in a combined elliptically polarized wave of variable angle and ellipticity, although in certain circumstances only one of the characteristic waves will return to the ground [47].

The Appleton-Hartree magneto-ionic model might be expected to apply equally to Es propagation. However, Es layers differ from the rest of the ionosphere in a number of significant ways, from their process of formation to the physical characteristics of the ionized E-region itself, and magneto-ionic propagation has never been conclusively demonstrated for VHF Es radio wave propagation. The differences are summarized in Table 1 [61]. The fact that they are so

dramatic suggests that the received characteristics of radio waves which have been reflected by an Es layer may be significantly different from those returned by the normal E region, even if the underlying processes are similar.

TABLE I
SUMMARY OF DIFFERENCES BETWEEN ES AND THE
NORMAL IONOSPHERIC E REGION

	E Region	Es
Formed by	Ionization of N ₂ , O ₂ , NO, O by solar EUV	Concentration of metallic ions by wind shear
Horizontal extent	1000s of km	Few to 100s of km
Thickness	~60 km	0.5 km to 5 km
Rate of refractive index variation	Gradual	Rapid
Electron density	Smoothly varying	Patchy
Mechanism of radio wave propagation	Mainly magneto-ionic double refraction	Magneto-ionic? Specular? Scatter?
Path length within the ionized layer	Long	Short

C. Empirical studies of Es radio wave propagation

Es reflections at vertical incidence are readily observed in ionosonde traces (see [14] for several examples). An Es layer may reflect 100% of the vertically-incident wave, in which case it is referred to as ‘blanketing’ Es, or it can be ‘non-blanketing’ i.e. semi-transparent, in which case reflections from higher ionospheric layers are also detectable at the same sounder frequency.

Oblique reflections of VHF signals from Es layers intermittently support propagation over ranges between approximately 500 km and 2500 km for a single reflection [11]. Received signals can be very strong and can even approach free-space values, but they often exhibit rapid and deep fading by as much as 60 dB [36]. It is likely that much of this fading is due to the limited size, non-uniform shape and rapid motion of the Es patches [3].

Reflections from Es layers can persist for hours, but other events are much shorter. One study found that 40% lasted for less than two minutes [48], another reported typical fading periods of five seconds [49]. Other studies have found that oblique-incidence Es reflections often consists of three or more components with different Doppler shifts and elevation/azimuth angles [50]. Experimental studies have also found the Maximum Usable Frequency (MUF) at oblique angles to be 1.5 times or even twice as large as values derived from the Es critical frequency according to the secant law [51]–[54], with significantly higher observed MUF for oblique Es reflections than would have otherwise been expected [55], [56].

Seasonal and diurnal variations in Es ionization intense enough to reflect frequencies in the VHF range broadly follow the same pattern as Es of a lower intensity, but with a sharper summer peak and lower incidence outside the peak season. A ten-year European Broadcasting Union program [36] monitored five transmitters on channels from 41 to 58 MHz as received via Es at 16 receiving stations around Europe. On average, a sharp peak was demonstrated in the May to August period each year with very little being observed after October or before April (although other studies have reported a minor winter peak

as well). VHF Es propagation was observed to be mainly a daytime phenomenon with peak activity around 12:00 and 18:00 local time at the midpoint of the path. Another extensive study [48], monitoring signals from broadcast transmitters around Europe in the range from 59 to 77 MHz, demonstrated very similar seasonal and diurnal patterns but with a lower frequency of occurrence and a more sharply defined summer peak as the frequency was increased. At the highest frequency they observed (77.25 MHz), diurnal variations exhibited a single evening maximum rather than also having a peak earlier in the day.

Systematic studies of the fading of signals propagated via mid-latitude Es have mostly been limited to vertical incidence in the medium frequency (MF) and HF ranges [12], [57], [58], but one study of oblique VHF Es propagation reported typical fading periods of between 2 and 20 seconds [59].

A number of experimental studies of the polarization of VHF waves by oblique Es reflection have been published, all written in the context of exploring whether polarization discrimination could help to protect VHF television reception from co-channel interference. The ten-year EBU study [36] referred to above concluded that the ionosphere clearly modifies the polarization of signals but that the component of the received signal with the same polarization as the transmitted wave was on average 5 dB stronger than the orthogonal component. By contrast, Edwards *et al.* [48] conducted an experiment which measured the horizontal and vertical components of a signal received in the UK via Es reflections from a horizontally-polarized transmitter in Poland on 70.31 MHz (a distance of just over 1500 km), over a period of four weeks in the summer of 1981. They found that signals on their two orthogonal receiving antennas were on average similar and their conclusion was that any polarization discrimination would be less than 2 dB. Ichinose & Kainuma [60] reported observations over the period May – August 1993 of Es reflections from a single 55 MHz television transmitter over an 1160 km path. Their results indicated that the received polarization was in general elliptical and the major axis of the ellipse deviated significantly from the transmitted polarization, which was horizontal. They identified two polarization fading groups: one consisting of small variations about the mean ellipse angle with a fading period of about ten seconds, and another slower variation over a much larger range of angles. The time resolution of their measurements was about half a second.

All three of these studies found that Es dramatically modifies the polarization of a linearly polarized transmitted signal in the process of reflecting it back to the ground. Our own previous research, published in 2019, presented high-speed amplitude measurements in two orthogonal polarization planes, using signals of opportunity received via Es reflection at 50 MHz [61]. Those initial measurements seemed to indicate that such signals tend to exhibit a strong axis of polarization which rotates over periods of seconds or minutes. The current research extends our earlier work by measuring both phase and amplitude, enabling full characterization of received polarization. This was not possible with the earlier technique.

III. EMPIRICAL RESEARCH

The amplitude and polarization characteristics of the received waves will exhibit different characteristics depending on the nature of the reflection mechanism:

- Scattering by small-scale irregularities in the ionosphere will cause rapid variations in received signal strength. Changes in ionization combined with relative movement between multiple scattering centers will lead to rapid and random focusing/defocusing and interference effects. For similar reasons, received polarization will vary rapidly and randomly.
- Specular reflection of a linearly polarized wave will result in received linear polarization which varies with the orientation of the reflecting surface. Signal fading will be relatively slow, corresponding to changes in Es-cloud shape and position.

- Magneto-ionic double refraction will result in polarization fading when the ionization is high enough to support both magneto-ionic components. It will potentially also exhibit, at the start and end of an Es event, the return to ground of the extraordinary wave only (analogous to the ‘Happy Hour’ effect observed at HF [47]), and/or deep fading due to interference between the ‘high ray’ and the ‘low ray’ [8, pp. 234-236].

We therefore suggest that wave polarization and fading may contain evidence of the Es radio wave propagation mechanism and we have designed our experiment accordingly.

In Europe, amateur radio operators have installed beacon transmitters for propagation research, operating at frequencies between 50.0 and 50.5 MHz. These beacons continuously transmit narrow-band signals with low power output, typically 1-10 Watts, and use omnidirectional antennas. A large number of such beacons are distributed over the continent. A subset of these beacons is selected for our research, each of them within the range 1400-2100 km from our measurement location at Churt in the south of England (51.135° N, 0.784° W), see Fig. 2. The minimum distance was selected both to reduce the possibility that other propagation modes were present and to increase the probability that Es propagation would occur, since MUF increases with increasing distance and therefore decreasing elevation angle [51], [54]. The maximum distance was chosen to reduce the likelihood of dual-hop propagation.

The Es propagation mechanism often produces only short intervals of 50 MHz radio propagation, from a few seconds to a few minutes. We monitor the beacon frequencies and make polarimetric measurements with a high sampling rate when Es propagation occurs. Raw recorded measurement data is then processed and compared with information from other scientific instruments and with predictions from advanced models.

On the map, two of the beacon locations, in Hungary and Spain at distances of 1,516 km and 1,644 km, are marked with red points. Recorded observations of these beacons will be analyzed and discussed in Section VIII to explain the process and to provide a proof of performance of the measurement system. The measurement system itself will be described in the next section.

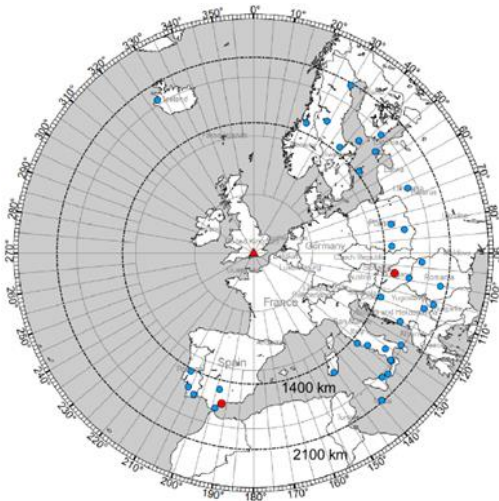


Fig. 2. Azimuthal map showing amateur radio 50 MHz beacon transmitters at distances between 1,400 and 2,100 km. The measurement location is marked with a red triangle and the beacons selected for initial analysis are marked with red dots. Background map courtesy Tom Epperly.

IV. MEASUREMENT SYSTEM DESIGN

To measure field strength and polarization, the measurement system consists of a pair of antennas, which separately capture two orthogonal polarization planes, and a directly digitizing dual-channel receiver.

With an expected Es cloud height between 90 and 130 km and assuming single-hop propagation, distances between 1400 and 2100 km will result in elevation angles below 7.5° [11]. Therefore, an antenna with a -1 dB vertical beamwidth of 15° would be optimal, which corresponds with a -3 dB beamwidth of 30°. Assuming negligible losses and a low sidelobe-level, the associated antenna gain can be estimated using [62]:

$$G = \log_{10} \left(\frac{41253}{30^\circ \times 30^\circ} \right) = 16.6 \text{ dBi} \quad (3)$$

If we allow 4 dB for ground gain, the preferred free space gain would be 12.6 dBi. We therefore selected a 7-element LFA antenna with an overall length of 9.6 m (1.6 λ) and a free space gain of 12.9 dBi. Two of these antennas are interlaced at right angles on one boom, to provide signal output for two orthogonal polarization planes, as shown in Fig. 3. To provide an uncluttered view towards the horizon, the antenna is mounted at 18 m (3 λ) above ground, on a tall triangular lattice tower. A fiberglass stub-mast is used between antenna and top of the tower to avoid distortion of the antenna’s radiation pattern, especially for vertical polarization. For the same reason, the feedlines are brought behind the reflector elements along the boom, after which they are brought down at some distance behind the elements. The antenna can be rotated electrically towards the desired beacon transmitter. The output of both antennas is brought down using Westflex 103 semi-air-spaced coaxial cable and connected to a dual channel receiver. The total attenuation of this cable, the balance transformer (balun) at the antenna and interconnecting cables is approximately 1.0 dB.

The LFA antenna is a loop-fed Yagi-Uda antenna with a slightly curved reflector element. It was designed to have low sidelobes, which is important for the reception of weak signals on 50 MHz, where ambient electromagnetic noise (‘radio noise’) from man-made devices is stronger than receiver noise. In Fig. 4, the vertical diagram of the LFA is compared with a conventional dipole-fed Yagi-Uda antenna of similar gain, both simulated using NEC4.2 [63], [64]. The difference in the sidelobe level is significant. The antenna height also helps to reduce received noise: doubling the antenna height reduces the received power of noise sources below the antenna by 6 dB.

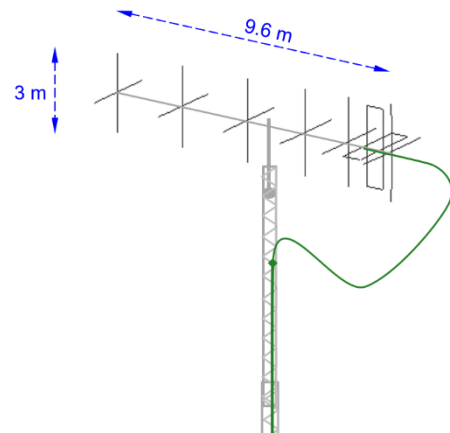


Fig. 3. The dual-polarization LFA antenna.

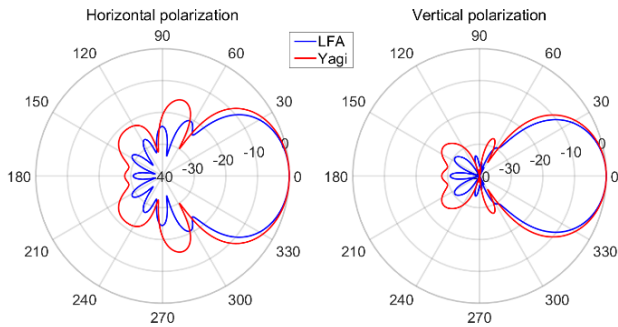


Fig. 4. Comparison of the normalized vertical radiation pattern of an LFA antenna (blue) and a traditional Yagi antenna of similar gain (red) in dB.

The receiver, an Apache Labs ANAN-8000DLE, samples both antenna inputs directly at the 50 MHz beacon frequency with a sampling speed of 122 MS/s. The digital data stream is filtered and down-sampled in an onboard Field Programmable Gate Array (FPGA) to obtain four 16-bit data streams at up to 192 kS/s, representing the in-phase and quadrature (IQ) components of the two sampled antenna voltages. The data stream is then again filtered to produce narrowband receivers at the beacon frequencies at selectable sampling speeds (here 6000 S/s of 32 bits/sample) and store the data on hard disk for post-processing. The polarization can be established on a per-sample basis from the amplitude and phase difference between the two antenna ports. This data rate and depth is sufficient to characterize fading, polarization, polarization dynamics and de-polarization. A block diagram of the entire system is shown in Fig. 5.

As the onset and ending of each propagation interval contains interesting information on the propagation mechanism, and low-power beacons are observed, a sensitive receiver is essential. This receiver, designed by a mixed open source group of radio amateurs, scientists and radio professionals, is optimized for stability, low phase noise and a high dynamic range. The receiver has a noise floor of -167 dBm/Hz. The narrow-band characteristics of the beacon signals also help to increase signal-to-noise ratio on reception. Measured differential phase and amplitude drift of the two antenna ports of the receiver is less than 0.2° and 0.05 dB over 24 hours. The measurement speed and accuracy of such modern hardware provides a step-change compared with older polarimetric Es research. However, while the differential phase bias drift is negligible, the absolute phase difference between the sampled antenna ports is a random number at start-up, which has to be calibrated away. This is typical of most software defined radio (SDR) receivers.

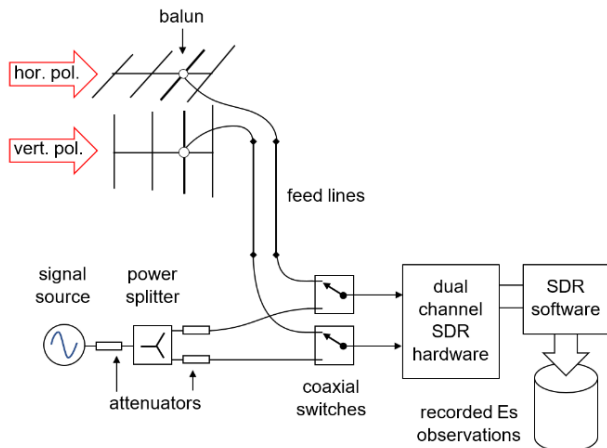


Fig. 5. Measurement system block diagram.

This number remains unaltered as long as the receiver settings are left untouched and the receiver is left powered on. For calibration, a stable signal source is fed to the receiver inputs via a power splitter and two high-quality coaxial changeover switches. Attenuators terminating the splitter ports in their characteristic impedance enhance the power and phase balance of the output ports, as depicted in the block diagram shown in Fig. 5. It suffices to inject this signal into the receiver prior to Es measurements and record it, then change over to the antenna and continue recording. The calibration signal can later be isolated from the recording and used to calibrate the measurement. It is good practice to repeat this calibration at the end of each recording to verify that no drift has occurred. The calibration values of all recordings give a good impression of the overall calibration drift of the receiver, which can be used to estimate the combined measurement uncertainty.

The attenuation and phase delay of all elements in the path between the antenna and receiver input – baluns, feedlines, interconnection cables, coaxial switches, filters – have been measured and corrected for. Also, the slight distance between the horizontal and vertical LFA antenna, mounted on a single boom, is determined and the resulting phase delay compensated for.

V. EXTERNAL FACTORS

Of course, the aim of the experiment is to measure the amplitude and polarization of the incoming wave alone. Both the absolute polarization and the variations in polarization hold information on the propagation mechanism. If external influences in the direct vicinity of the measurement system modify the polarization, to avoid false interpretation it is important to know whether that influence can cause dynamic polarization changes and what the magnitude of those changes may be.

Interference from electrical appliances (‘radio noise’) can easily be discerned from the beacon signal, which has a very stable known frequency and is periodically modulated to provide a station identification. The influence of buildings and trees is harder to measure, but as the antenna is mounted well above them and an antenna with a very clean antenna pattern has been selected, this influence is believed to be negligible. It was verified that tree movement caused by wind had no observable influence on the measurements by observing a stable line-of-sight signal.

However, despite its directivity and clean pattern, the vertical half-power beamwidth of the antenna exceeds 30°. This implies that the antenna not only sees the direct wave arriving from the ionosphere, but it also sees a component that is reflected by the ground further out. The interference between the direct and the reflected wave cause an elevation-angle dependent interference pattern. A slowly reducing Es layer height [21] will cause a gradually decreasing elevation angle. If this passes a minimum in the interference pattern, substantial changes in amplitude and phase angle will occur. As this effect is dissimilar for horizontal and vertical polarization as explained below, important changes in the measured polarization may occur even if the polarization of the incoming wave itself is constant. This observation could be mistaken for a property of the propagation mechanism, whereas in fact it is a product of the combination of the local environment and the changing Es height. This aspect has been ignored in previous literature.

If this effect is not mitigated or compensated for, the measured polarization may differ substantially from the real polarization of the incoming wave. Therefore, in this section, the impact of the ground reflection will be investigated, to establish conditions that will provide accurate polarization measurements.

A. Perfect electric conductor ground

We will start with a simple geometric optics 2-ray model. This model assumes that both the direct and reflected waves are plane waves that can be represented as a single ray perpendicular to the wave front. This approach is realistic enough to give an initial insight into the interference mechanism, but it ignores near-field effects and also represents the antenna as a point source. Therefore our analysis in Section VI, in which we derive the precise bias values for the specific antenna system that is used in our experiment, is based on a full-wave model of the real antenna and ground reflections, including near-field effects.

In the 2-ray model, assuming a flat and level ground surface, the difference in path length between the direct and reflected wave can be calculated using trigonometry. This is depicted in Fig. 6, where $l_2 - l_1$ is the path length difference, h the antenna height, and α the elevation angle. For a perfect electric conductor (PEC) ground, the reflection coefficient ρ is 1 for vertical polarization and $e^{j\pi}$ for horizontal polarization. When λ is the wavelength, the resulting phase difference for horizontal (H) and vertical polarization (V) can be expressed as:

$$\text{H: } \Delta\varphi = \frac{2\pi h}{\lambda} \frac{\{\cos(2\alpha) - 1\}}{\sin \alpha} + \pi \quad (4)$$

$$\text{V: } \Delta\varphi = \frac{2\pi h}{\lambda} \frac{\{\cos(2\alpha) - 1\}}{\sin \alpha} \quad (5)$$

The ground gain factor K , can be written as:

$$K(\alpha) = 1 + e^{j\Delta\varphi} \quad (6)$$

Because the horizontal component experiences an additional phase shift of π compared with the vertical component, the interference patterns vs elevation angle for the two components do not align - as shown in Fig. 7 for antenna height $h = 3\lambda$. At certain elevation angles only one polarization is received and, at the angles in between, both amplitudes vary rapidly with elevation angle. The observed relationship between the horizontal and vertical components at the antenna does not, therefore, accurately represent the free space polarization of the incoming wave.

B. Lossless dielectric ground

While this simple model demonstrates the problem, it represents the extreme case of a perfect ground reflection. As a next step the ground will be modelled as a perfect dielectric (PD). According to Kraus [65], the ground reflection coefficient ρ now becomes:

$$\text{H: } \rho = \frac{E_r}{E_i} = \frac{\sin \alpha - \sqrt{\epsilon_r - \cos^2 \alpha}}{\sin \alpha + \sqrt{\epsilon_r - \cos^2 \alpha}} \quad (7)$$

$$\text{V: } \rho = \frac{E_r}{E_i} = \frac{\epsilon_r \sin \alpha - \sqrt{\epsilon_r - \cos^2 \alpha}}{\epsilon_r \sin \alpha + \sqrt{\epsilon_r - \cos^2 \alpha}} \quad (8)$$

where E_i and E_r are the electric field strengths of the incident and reflected wave and ϵ_r is the relative permittivity of the ground plane. From the numerator of (8), an angle can be identified at which no reflection of the vertically polarized component occurs, which is known as the 'Brewster angle' [65, 66]:

$$\alpha_B = \tan^{-1} \left(\frac{1}{\sqrt{\epsilon_r}} \right) \quad (9)$$

Fig. 8 shows the relationship between the dielectric constant ϵ_r and the Brewster angle α_B . The relative dielectric constants of poor, average, good ground and sea water (see Table II) are marked in the graph. The reflection coefficient now has become a function of the elevation angle; its magnitude and phase are shown in Fig. 9.

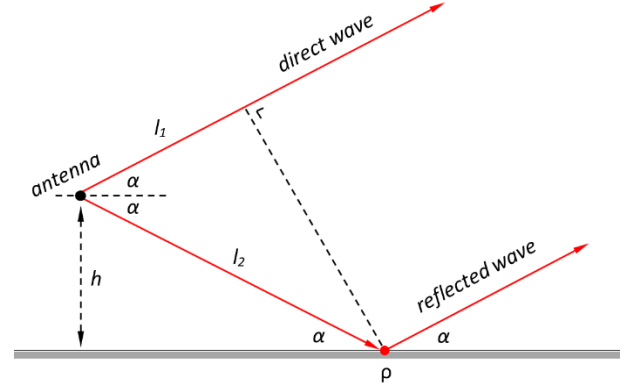


Fig. 6. Geometry of the ray paths of the direct and reflected waves.

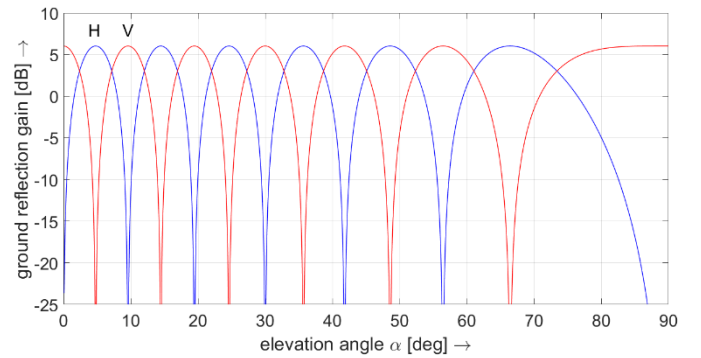


Fig. 7. Interference patterns of a point source 3λ above a perfect electric conductor (PEC). Blue is horizontal polarization, red is vertical polarization.

TABLE II
BREWSTER ANGLE FOR TYPICAL GROUND TYPES

	ϵ_r	α_B
poor gnd	5	24.1°
avg gnd	13	15.5°
good gnd	17	13.6°
sea water	81	6.3°

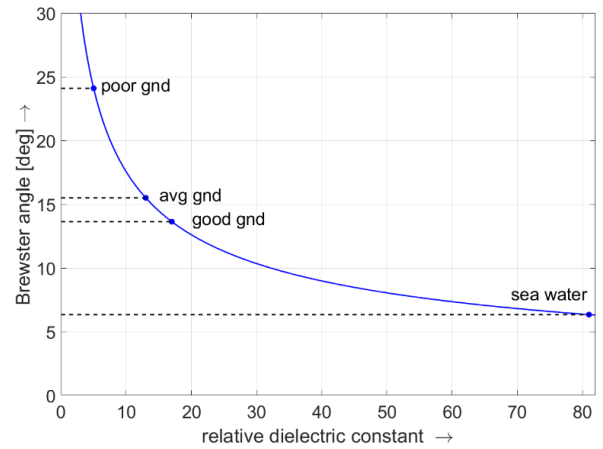


Fig. 8. Relationship between dielectric constant and Brewster angle.

C. Lossy non-magnetic dielectric ground

To further improve the ground model, we now include the ground losses. According to Kraus [65] and Jordan [67], the reflection coefficient ρ of a lossy non-magnetic dielectric (LND) ground is:

$$\text{H: } \rho = \frac{E_r}{E_i} = \frac{\sin \alpha - \sqrt{(\epsilon_r - j \frac{\sigma}{\omega \epsilon_0}) - \cos^2 \alpha}}{\sin \alpha + \sqrt{(\epsilon_r - j \frac{\sigma}{\omega \epsilon_0}) - \cos^2 \alpha}} \quad (10)$$

$$\text{V: } \rho = \frac{E_r}{E_i} = \frac{(\epsilon_r - j \frac{\sigma}{\omega \epsilon_0}) \sin \alpha - \sqrt{(\epsilon_r - j \frac{\sigma}{\omega \epsilon_0}) - \cos^2 \alpha}}{(\epsilon_r - j \frac{\sigma}{\omega \epsilon_0}) \sin \alpha + \sqrt{(\epsilon_r - j \frac{\sigma}{\omega \epsilon_0}) - \cos^2 \alpha}} \quad (11)$$

The magnitude and phase angle of the reflection coefficient are shown in Fig. 10. While the reflection coefficient no longer vanishes, there is still a distinct minimum for vertical polarization at the ‘pseudo-Brewster angle’ [68], which can be calculated as follows [69]:

$$\alpha = \left(\frac{n_0^2}{n^2 + k^2} \right)^2 + \frac{1}{9} \quad (12)$$

$$\beta = \left(\frac{n_0^2}{n^2 + k^2} \right)^3 \left(\frac{n^2 - k^2}{n^2 + k^2} \right) + \frac{1}{27} \quad (13)$$

$$B = \sqrt{\alpha} \cos \left[\frac{1}{3} \cos^{-1} \left(\frac{\beta}{\alpha^2} \right) \right] + \sqrt{3} \alpha \sin \left[\frac{1}{3} \cos^{-1} \left(\frac{\beta}{\alpha^2} \right) \right] - \frac{1}{3} \quad (14)$$

$$\alpha'_B = \tan^{-1}(\sqrt{B}) \quad (15)$$

where α'_B is the pseudo-Brewster angle expressed as an elevation angle, n_0 the refractive index of air, and n and k the real and complex parts of the refractive index of the ground. Both n and k can be derived from the ground parameters using [65]:

$$n^2 = \epsilon_r \quad (16)$$

$$k^2 = \frac{\sigma}{2\pi f \epsilon_0} \quad (17)$$

Values of α'_B for typical ground types at the observation frequency used in our experiment, $f = 50$ MHz, can be found in Table III. It can be seen that except for sea water, this angle is only slightly lower than the Brewster angle.

D. Polarization measurement below the pseudo-Brewster angle

The interference patterns for PD and LND ground are shown in Fig. 11. Above the (pseudo-)Brewster angle, the phase difference between horizontal and vertical polarization approaches π radians, and the interference patterns remain complementary. The extent of the minima and enhancements are less pronounced than for PEC ground (Fig. 7), as the magnitude of the reflection coefficient is smaller.

Below the (pseudo-)Brewster angle, however, the phase difference between horizontal and vertical polarization vanishes and the interference patterns synchronize. As a result of this, the amplitude difference between horizontal and vertical polarization, and its variation with elevation angle, decreases significantly.

From this investigation, we may conclude that polarization measurements of incoming waves arriving at low but varying angles can only be measured with reasonable accuracy below the pseudo-Brewster angle, and only if the biases caused by the ground reflection are compensated for.

TABLE III
PSEUDO-BREWSTER ANGLE AT 50 MHz
FOR TYPICAL GROUND TYPES

	σ	ϵ_r	α_B	α'_B
poor gnd	1 mS/m	5	24.1°	23.6°
avg gnd	5 mS/m	13	15.5°	14.7°
good gnd	15 mS/m	17	13.6°	12.1°
sea water	5 S/m	81	6.3°	1.3°

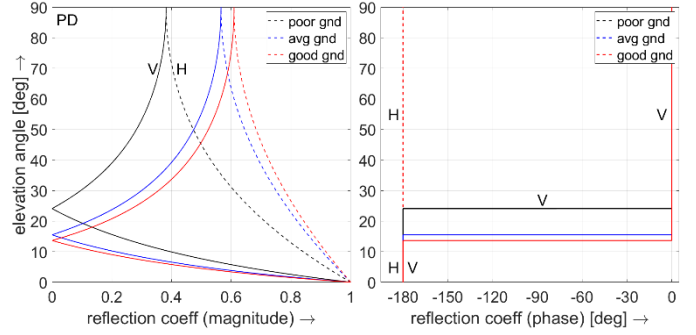


Fig. 9. Magnitude and phase of the reflection coefficient for perfect dielectric (PD) ground. Dashed lines are horizontal polarization, solid lines vertical polarization. For vertical polarization, a phase reversal occurs at the Brewster angle.

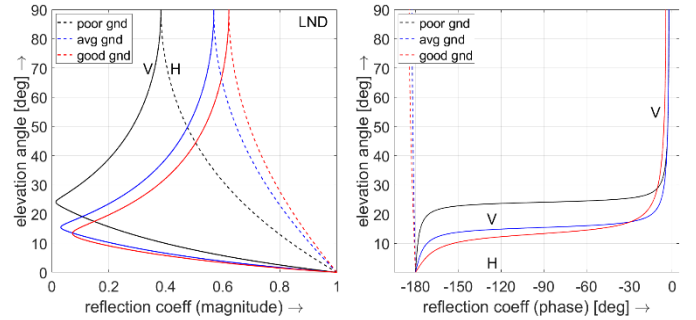


Fig. 10. Magnitude and phase of the reflection coefficient for a lossy non-magnetic dielectric (LND) ground. Dashed lines are horizontal polarization, solid lines vertical polarization. The pseudo-Brewster angle is slightly lower

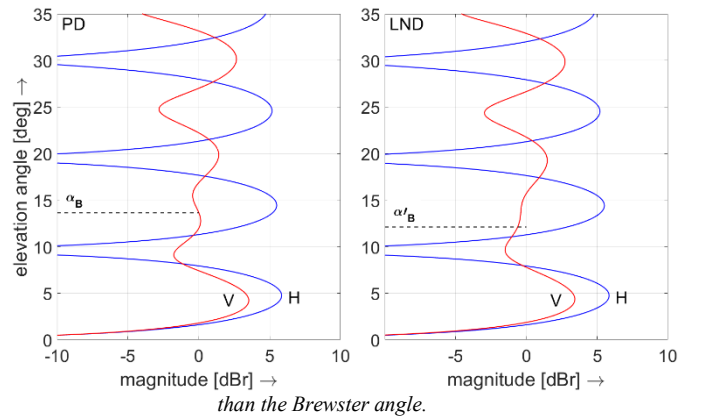


Fig. 11. Interference pattern of a point source 3λ above (left) a perfect dielectric (PD) ground, with $\epsilon_r = 17$ and (right) a lossy non-magnetic dielectric (LND) ground, with $\sigma = 15$ mS/m, $\epsilon_r = 17$. Horizontal polarization is blue, vertical polarization is red.

E. Optimum antenna height

To realize the widest range of elevation angles in which the ground-reflection induced biases are small, the first null of the interference pattern must be higher than the pseudo-Brewster angle. The corresponding maximum antenna height can be derived from the PEC case and (4):

$$\frac{\pi h_{max}}{\lambda} \frac{\{1-\cos(2\alpha'_B)\}}{\sin \alpha'_B} = \pi \leftrightarrow \quad (18)$$

$$h_{max} = \lambda \frac{\sin \alpha'_B}{\{1-\cos(2\alpha'_B)\}} \quad (19)$$

Based on (19), for average ground a maximum antenna height of 2 λ is optimal, see Table IV. In our measurement location, a greater height was needed to realize an uncluttered view so a compromise height of 3 λ was chosen, resulting in a first null at 9.5°. For our experiments this is acceptable because the majority of our monitored Es signals arrive at elevation angles below 7.5°.

VI. DETERMINATION OF GROUND REFLECTION BIASES

In polarization measurement, a point often ignored is that the ground reflection causes both amplitude and phase biases that are different for horizontal and vertical polarization. This can cause errors. Fortunately, when measuring waves that arrive below the pseudo-Brewster angle, the biases caused by the ground reflection vary relatively slowly with elevation angle. Therefore, if we know the range of elevation angles of the incoming waves, we can compensate for these biases in our polarization measurements, provided we can model them with sufficient accuracy.

A. NEC 4.2 simulations

In the previous section, a 2-ray model was used to illustrate the role of the ground reflection, assuming a point source as the antenna. In reality, the selected antenna is 1.6 λ long and installed at a height of 3 λ and part of the ground reflection therefore occurs in the near field of the antenna. Furthermore, the beamforming of a Yagi-Uda end-fire array is based on the amplitude and phase relationship between the excited and parasitic elements and its overall phase delay changes when the angle is offset from boresight. Therefore, it is not sufficient to multiply the antenna radiation pattern with the interference pattern of the ground reflection. A full-wave simulation of the combination of antenna and ground is necessary to precisely establish the bias values. As we measure polarization by observing the amplitude and phase difference in two polarization planes, we are mainly interested in the differences in antenna gain and phase delay of the horizontally and vertically polarized waves. The simulations are performed with the Numerical Electromagnetics Code (NEC) method-of-moments software [63], [64] version 4.2, using a Sommerfeld ground model [70]. The vertical radiation pattern of the antenna, including the ground reflection, is simulated in the azimuthal direction of maximum radiation. For consistency, the same three ground types (poor, average, and good) are investigated. The results are shown in Figs. 12, 13 and 14 assuming flat, level ground. Each graph consists of 4 subgraphs.

TABLE IV
UPPER ANTENNA HEIGHT LIMIT FOR TYPICAL GROUND TYPES

	σ	ϵ_r	α'_B	h_{max}
poor gnd	1 mS/m	5	23.6°	1.2 λ
avg gnd	5 mS/m	13	14.7°	2.0 λ
good gnd	15 mS/m	17	12.1°	2.4 λ
sea water	5 S/m	81	1.3°	22 λ

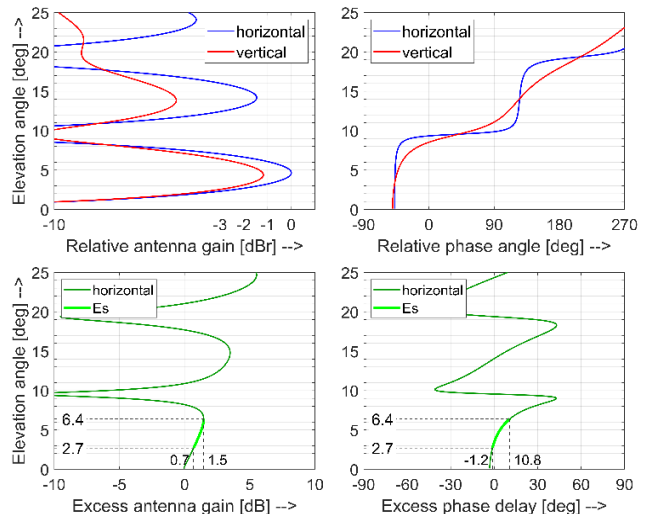


Fig. 12. Magnitude and phase vs. elevation angle. NEC 4.2 simulation, poor ground, $\sigma = 1$ mS/m, $\epsilon_r = 5$; pseudo-Brewster angle 24°. Marked angle range: see text.

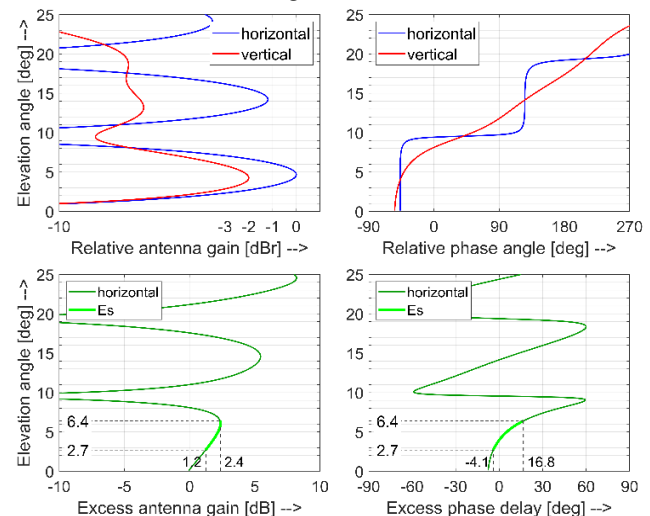


Fig. 13. Magnitude and phase vs. elevation angle. NEC 4.2 simulation, average ground, $\sigma = 5$ mS/m, $\epsilon_r = 13$; pseudo-Brewster angle 15°. Marked angle range: see text.

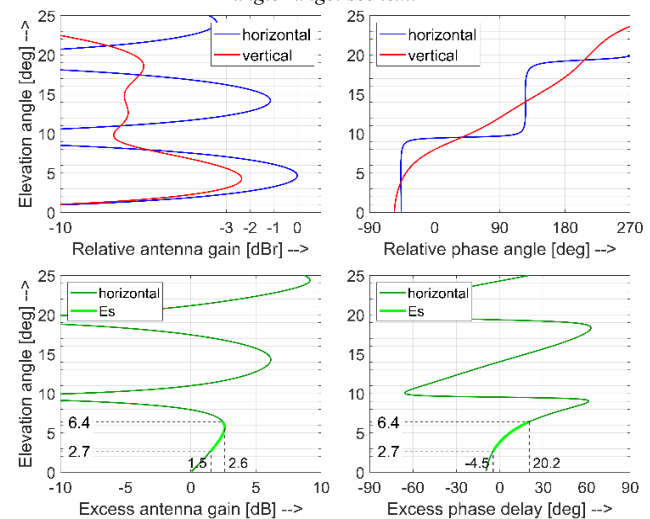


Fig. 14. Magnitude and phase vs. elevation angle. NEC 4.2 simulation, good ground, $\sigma = 15$ mS/m, $\epsilon_r = 17$; pseudo-Brewster angle 12°. Marked angle range: see text.

In each case, the top-left subgraph shows the normalized antenna gain for horizontal and vertical polarizations, up to 25° elevation angle. The interference patterns can be clearly seen, with the first null at 9.5°. The top-right subgraph shows the phase angles of the horizontally and vertically polarized waves. The bottom-left subgraph shows the excess antenna gain for the horizontally polarized wave over the vertical one. The bottom-right subgraph shows the excess phase delay of the horizontally polarized wave over the vertical one.

To illustrate the elevation range of most interest, minimum and maximum angles of 2.7° and 6.4° are marked, corresponding to Es virtual reflection heights from 90 km to 130 km and single-hop distances from 1,500 km to 1,650 km [11].

In Fig. 12, representing poor ground, the pseudo-Brewster angle is 24°, and the lobes of the vertical radiation pattern for horizontal and vertical polarization overlap. In Fig. 13, representing average ground, the pseudo-Brewster angle is 15°; below that angle the lobes coincide, but above that angle they become complementary. This transition point is slightly lower in Fig. 14, which represents good ground and for which the pseudo-Brewster angle is 12°.

The key range of bias values is expanded in Fig. 15. The left-hand subgraph shows the excess antenna gain for the horizontally polarized wave over the vertical. The right-hand subgraph shows the excess phase delay of the horizontally polarized wave over the vertical.

B. Verification with FEKO simulations

In order to increase confidence in the results of the antenna modelling, it was decided to repeat the analysis using an alternative simulation package. For this we used Altair FEKO™ (version 2018.2.1), which is a hybrid package with several implemented methods, of which we used the method-of-moments solver.

Comparison of the output from the two simulations clearly shows some differences between FEKO and NEC 4.2. While the radiation pattern is practically identical in the main lobe and the suppression of the sidelobes is similar, the position and magnitude of the sidelobes are different. Despite this, as shown in Table V, the difference in amplitude and phase biases is very small: less than 0.1 dB and 0.9°.

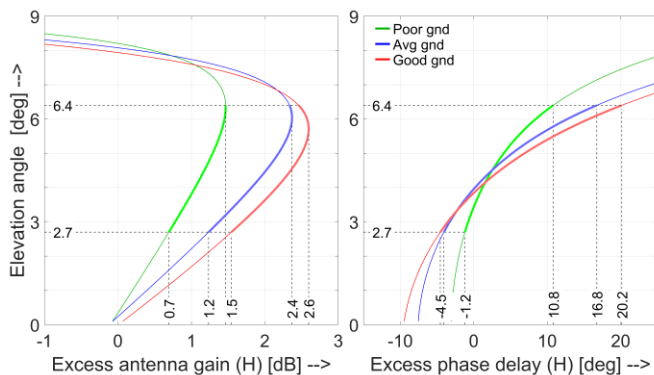


Fig. 15. Expanded view of simulated gain (left) and phase (right) bias values for flat, level ground (NEC4.2). Marked angle range: see text.

TABLE V
COMPARISON OF RESULTS FROM NEC 4.2 AND FEKO SIMULATIONS

	NEC 4.2		FEKO	
	2.7° to 6.4°	2.7° to 6.4°	2.7° to 6.4°	2.7° to 6.4°
poor gnd	0.7 to 1.5 dBr	-1.2 to 10.8°	0.8 to 1.6 dBr	-1.9 to 10.1°
avg gnd	1.2 to 2.4 dBr	-4.1 to 16.8°	1.3 to 2.5 dBr	-4.7 to 15.9°
good gnd	1.5 to 2.6 dBr	-4.5 to 20.2°	1.6 to 2.7 dBr	-5.2 to 19.3°

Subsequently, the effect of the antenna mast below the antenna was also simulated in FEKO. The antenna itself is isolated from the mast by a 2.12 m long fiberglass pole extending above the triangular lattice mast, which is 178 mm per side. In the model, the mast retains the same cross-section along its entire length. Three scenarios were tested: one without the mast, one with the mast grounded, and one with the mast isolated from the ground. The difference between these three scenarios is very small: less than 0.1 dB and 0.8°.

The mean bias caused by these external influences will be corrected for in the overall system calibration, which is done in the post-processing, and the residual variations around that value will be accounted for in the measurement uncertainty analysis.

VII. POST-PROCESSING, CALIBRATION AND MEASUREMENT UNCERTAINTY

Retention of the original high-rate digital IQ samples for later processing allows a wide range of analysis approaches to be applied without loss of fidelity. The analysis undertaken so far is focused on characterizing the aggregate polarization of the beacon signals, although other investigations are also under development.

The key steps during post-processing are shown in Fig. 16 and described below.

A. Beacon signal extraction

First, a single complex amplitude is calculated from each pair of I and Q samples for each channel (i.e. each orthogonal polarization). The raw samples are then plotted v/s time to allow the useful time segment(s) of the recording to be identified (Step 1). The time series from these selected time segments are then converted into waterfall spectrograms using a fast Fourier (FFT) transform with a Blackman-Harris window. This allows the precise frequencies of the beacon signal(s) and the calibration signal to be measured (Step 2). ‘Empty’ frequencies in the spectrogram are also identified, at which the ambient noise level can be measured. This information is then used to extract the beacon, calibration and noise data for the desired time segment, each filtered with a 25 Hz bandwidth (Step 3). The beacon signals consist of a continuous carrier that is periodically replaced with a station identification in Morse code, either by on-off keying or frequency shift keying (FSK). When FSK is used, the ‘mark’ and ‘space’ frequency components are filtered using separate 25 Hz filters, after which their complex amplitudes are recombined.

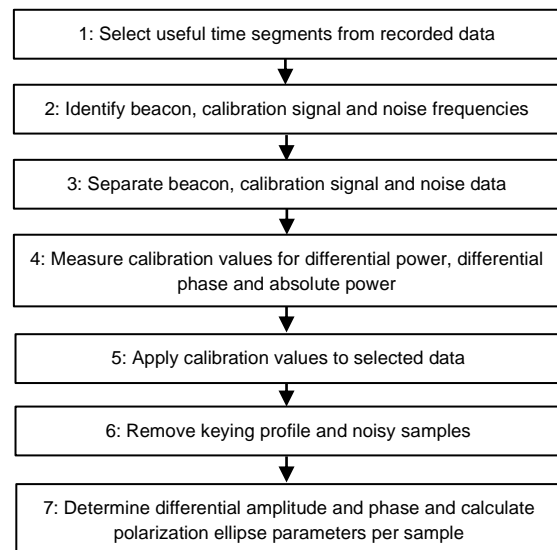


Fig. 16. Filtering, calibration and post-processing steps.

B. Calibration of the recorded measurements

The data stream containing the calibration signal for the segment is then processed (Step 4) to derive correction factors to compensate for receiver offsets and drift, including differential amplitude, differential phase, and absolute power. These correction factors are then applied to the filtered beacon data stream(s) (Step 5), along with static corrections for differential antenna cable loss and phase lag, and ground reflection corrections as derived in Section VI.

C. Noise filtering and polarization calculations

As the beacon signals are subject to fading, not all the samples have sufficient signal-to-noise ratio to provide accurate measurements. Therefore, in Step 6, samples which are less than 10 dB above the average ambient noise level on either channel are removed using a ‘noise squelch’ function, acting on the noise level established in Step 3. An additional ‘dynamic squelch’ removes as much as possible of the beacon’s keying profile by deleting samples which are more than a threshold level (3 – 10 dB) below the moving average on that channel. These two mechanisms operate sequentially on each of the two data streams, with the aim of ensuring that results are not calculated based only on noise.

Finally, in Step 7, the desired polarization-related parameters are calculated from the filtered, calibrated and cleaned data. The power ratio and the phase difference between the vertical and horizontal signals are directly measured and the characteristics of the polarization ellipse are calculated from them. Following Mott [72] and Stutzman [73] and aligning with the IEEE standard definitions for polarization parameters [74], [75] gives for the axial ratio ar and tilt angle τ :

$$ar = -\cot\left(\sin^{-1}\left(\frac{2P \sin \varphi}{1+P^2}\right)/2\right) \quad (20)$$

$$\tau = \tan^{-1}\left(\frac{2P \cos \varphi}{1-P^2}\right)/2 \quad (21)$$

$$\text{If } P > 0, \tau = \tau - \text{sgn}(\tau) * \frac{\pi}{2} \quad (21a)$$

where P is the ratio of the vertical field strength to the horizontal field strength and φ is the phase difference between the two fields (positive = vertical leads). The calculated tilt angle is relative to the horizontal, with positive angles defined clockwise as seen in the direction of travel.

D. Measurement uncertainty

After calibration, the residual measurement uncertainty is estimated following the guidelines in the ISO ‘Guide to the Expression of Uncertainty in Measurement’ (GUM) [71]. As the direct measurements are of differential signal power and phase, their uncertainties are first established, after which the uncertainty of the polarization parameters is derived from them. The measurement uncertainty estimates for differential power are summarized in Table VI and for differential phase in Table VII. The values in the tables and the discussion below relate to observations of the Hungarian beacon (see Section VIII) but the overall estimates are similar for both of the examples analyzed in this article.

The mean value in the table represents the bias that has been compensated for in the calibration and does not contribute to the measurement uncertainty. Note that all estimates are on a per-sample basis (normally at 6000 S/s) without averaging. The following sources of uncertainty are identified:

- *Measured power and phase:* uncertainty is introduced into the power and phase measurements by ambient antenna noise within the selected bandwidth. The effect of antenna noise at the receiving site has been measured by injecting a calibration signal into each of the two antenna feedlines with the antennas receiving

ambient noise from the direction of the Hungarian beacon. Figs. 17 and 18 show measured uncertainty, for power ratio and phase difference respectively, against a typical range of per-channel (signal + noise)/noise ratios. Polynomial regression lines are also shown, to aid interpretation. For the purpose of the overall uncertainty calculations in Tables VI and VII, estimates of 0.5 dB and 3.2° have been adopted, corresponding to a target (signal + noise)/noise ratio of 25 dB.

- *Power and phase difference calibrations:* the internal variability in the calibration measurement is very small (typically <0.01 dB for power and <0.1° for phase) but results are also dependent on any imbalance in the combination of power splitter, attenuators, cables and connectors, which has been measured to total less than 0.1 dB for power and 0.6° for phase.
- *Main feedline differential loss and phase delay* have been measured to an accuracy of <0.5 dB for attenuation and 0.6° for phase lag. These values include the attenuation and delay in baluns and antenna connectors.
- *Mismatch loss:* power and phase errors due to any potential mismatch between the antenna, the cable and the receiver are difficult to compensate for and are therefore treated purely as a source of uncertainty. The standing wave ratio on the two antenna cables has been measured to be 1.4:1 or less in each case, corresponding to a maximum of 17 % reflected power. Based on this, a maximum mismatch loss of 0.1 dB and mismatch phase error of 0.5° have been calculated.
- *On-axis antenna gain and phase* characteristics of the individual antennas may differ by up to 1 dB and 10° from simulated values due to uncertainty in modelling. On that basis, but taking account of the fact that the antennas are of identical materials and construction (the principal sources of modelling errors), the characteristics of the two antennas are estimated to differ by less than 0.7 dB and 5°.

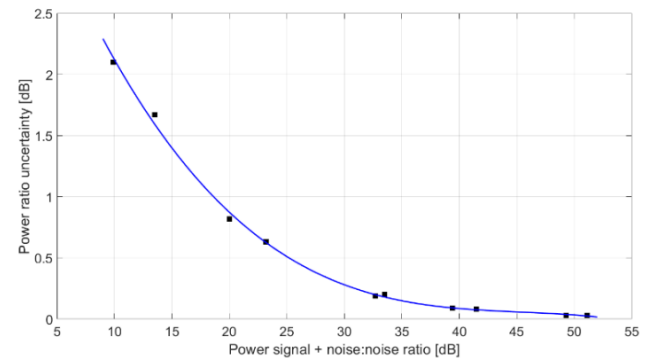


Fig. 17. Measured power ratio uncertainty (standard deviation) at the receiving site versus single-channel (signal + noise)/noise ratio.

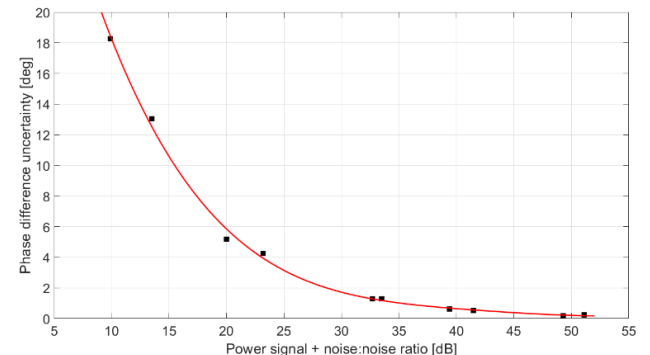


Fig. 18. Measured phase difference uncertainty (standard deviation) at the receiving site versus single-channel (signal + noise)/noise ratio.

- *Antenna off-axis bias*: NEC-4 modelling indicates that signal deviations off-axis, due either to errors in antenna pointing or to Es reflection via indirect paths [45], could cause additional biases of up to 1 dB in gain and up to 2° in phase for a 15° azimuth deviation from the true direction to the beacon.
- *Ground reflection bias*: due to Es reflection height uncertainty, a range of possible elevation angles must be considered. Using the HG7BVA beacon as an example (see Section VIII), including uncertainty in the ground characteristics, the residual uncertainties after correction of the mean for ground reflection are 0.5 dB and 3°. Extra allowances of 0.5 dB in gain and 0.5° in phase are also added for modelling uncertainty, so the resulting total estimated uncertainties for ground reflection bias are 1.0 dB and 3.5°.

An overall expanded standard uncertainty has been estimated for each of the two measurements, representing a 95% confidence interval. The overall per-sample measurement uncertainties in power ratio and phase difference are estimated to be 2.1 dB and 12.8°.

Application of equations (20), (21) and (21a) allows the calculation of axial ratio and tilt angle for any combination of differential power and phase and also permits estimation of the uncertainties in calculated ellipse parameters. The equations are highly non-linear so to quote generic uncertainties would be meaningless, but a specific example can be given based on the analysis described in Section VIII.

Power ratio and phase difference measurements of -10 dB (V/H) and -50° (V-H) correspond to an ellipse with an axial ratio of 4.3 and a tilt angle of 12.2°, similar to the central part of Figs. 21 and 22. Each measured parameter affects both ellipse parameters, so their uncertainties must be combined. For this example, treating the uncertainties as independent, the per-sample expanded standard uncertainty (95% confidence) in axial ratio is estimated to be 1.3 and in tilt angle 4.3°.

TABLE VI
MEASUREMENT UNCERTAINTY ESTIMATION FOR POWER RATIO

Source of uncertainty	Mean dB	Uncertainty dB	Uncertainty %	Probability distribution	Divisor	Standard uncertainty %
Receiver						
Measured power ratio	0	0.5	12	normal	1	12
Power difference calibration	0.3	0.1	2	uniform	1.732	1
Antenna cable						
Main feed lines differential loss	-0.7	0.5	12	uniform	1.732	7
Mismatch loss	0	0.1	2	u-shaped	1.414	2
Antenna						
Antenna on-axis gain bias	0	0.7	17	normal	1	17
Antenna off-axis gain bias	0	1.0	26	uniform	1.732	15
Ground reflection						
Ground reflection gain bias	1.5	1.0	26	uniform	1.732	15
Total						
Combined standard uncertainty				normal		31 %
Expanded standard uncertainty (95% confidence)				normal (k=2)		62 % 2.1 dB

TABLE VII
MEASUREMENT UNCERTAINTY ESTIMATION FOR PHASE DIFFERENCE

Source of uncertainty	Mean deg	Uncertainty deg	Probability distribution	Divisor	Standard uncertainty deg	
Receiver						
Measured phase difference	0	3.2	normal	1	3.2	
Phase difference calibration	0	0.6	uniform	1.732	0.3	
Antenna cable						
Main feed lines electrical length	-6.6	1.0	uniform	1.732	0.6	
Mismatch phase change	0	0.5	u-shaped	1.414	0.4	
Antenna						
Antenna on-axis phase bias	0	5.0	normal	1	5.0	
Antenna off-axis phase bias	0	2.0	uniform	1.732	1.2	
Ground reflection						
Ground reflection phase bias	-2.7	3.5	uniform	1.732	2.0	
Total						
Combined standard uncertainty				normal		6.4
Expanded standard uncertainty (95% confidence)				normal (k=2)		12.8 deg

VIII. DEMONSTRATION OF SYSTEM PERFORMANCE

A large number of observations of beacon signals arriving via Es propagation were recorded from May to August in 2018. To demonstrate system performance, two recordings of Es propagation are analyzed and presented here. Two specific beacons have been chosen so that the paths are at roughly 90° to each other and therefore have significantly different orientations relative to the earth’s magnetic field. This aspect is particularly interesting when the importance of magneto-ionic propagation is considered. One of the beacons, identified as ‘HG7BVA’ and transmitting at 50.430 MHz, is in Hungary and the other, identified as ‘ED7YAD’ and transmitting at 50.475 MHz, is in Spain. Their positions are shown on the azimuthal map in Fig. 2.

A. Propagation path Hungary – United Kingdom

The first beacon, HG7BVA in Hungary (47.412° N, 19.387° E), is at a distance of 1,516 km from the measurement location in the south of England (51.135° N, 0.784° W). The bearing, as seen from the receiver, is 98°. Assuming a single-hop direct path, the reflection point will be located near 49.3° N, 9.3° E. At the reflection point, assuming a height of 110 km in the ionosphere, the declination and inclination of the magnetic field are respectively 2.5° and 64.9°, according to the International Geomagnetic Reference Field (IGRF) model [78]. The angle between the downward wave and the Earth’s magnetic field is therefore between 91° and 93°, and the Quasi-Transverse (QT) approximation of the polarization equation (2) holds; the limiting polarization would therefore be expected to be elliptical approaching linear [2, pp.75-76].

As discussed in Section V, to accurately measure the polarization of the incoming wave, the influence of the ground effect has to be compensated for. The profile of the ground reflection area towards HG7BVA (approximately the first Fresnel zone) contains mixed terrain including fields, trees, and a few buildings and has an overall upward slope of about 1.6° to the horizontal. The upward slope will have the effect of tilting the vertical radiation pattern upward by the same amount and this has been compensated for in determining the amplitude and phase bias corrections to be applied. There is a small but deep depression (about 5.5 m deep) at 250 m along the path towards the beacon but its size relative to the total reflection area, which stretches up to several km from the receiving site depending on the elevation angle, is judged small enough not to have a major effect on the ground reflection [76], [77].

As described in Section II, Es layers can occur at heights between 90 km and 130 km and at this stage the actual height for the Es events in question is not known. For observations of HG7BVA, at a distance of 1,516 km, the range of possible elevation angles is between approximately 3.6° and 6.4° [11]. Using the bias graphs of Fig. 15, making allowance for the ground tilt, assuming ‘average ground’ and taking account of the likely range of elevation angles, gives ground reflection correction factors of +1.5 dB ± 0.5 dB in amplitude and -2.7° ± 3° in phase.

B. Propagation path Spain – United Kingdom

The second beacon, ED7YAD in southern Spain (36.606° N, 4.595° W), is at a distance of 1,644 km from the measurement location on a bearing of 192°. Assuming a single-hop direct path, the reflection point will be located near 43.9° N, 2.7° W and elevation angles will be between approximately 2.7° and 5.4°, corresponding to Es layer heights of 90 km - 130 km [11]. At the reflection point, assuming a height of 110 km in the ionosphere, the declination and inclination of the magnetic field are respectively -0.6° and 59.1°, according to the

IGRF model. The angle between the downward wave and the Earth's magnetic field is therefore between 63° and 65° , and the QT approximation is no longer valid.

The profile of the ground reflection area towards ED7YAD consists largely of fields plus some trees, with an overall upward slope of about 3.6° to the horizontal. Once again, the upward slope has been compensated for in determining the amplitude and phase bias corrections to be applied. There are only minor deviations from flatness along the reflection area [76], [77] although there is some terrain shadowing beyond 750 m. This will block the lower Es elevation angles, which reduces the range of observable Es layer heights. Using the bias graphs of Fig. 15, making allowance for the ground tilt, assuming 'good ground' and taking account of the likely range of elevation angles, gives ground reflection correction factors of $+0.6 \text{ dB} \pm 0.5 \text{ dB}$ in amplitude and $-8.0^\circ \pm 1.5^\circ$ in phase for observations of ED7YAD.

C. Analysis of the observations

The data from the selected recordings is filtered and calibrated as described in Section VII. Example plots, representing initial results and demonstrating the performance of the measurement system, are shown in Figs. 19 through 22 (Hungary-UK) and 23 through 26 (Spain-UK).

The first two graphs of each series of four show the information that is measured directly: the signal power in two orthogonal polarization planes, and the phase difference between them. The signal power graphs provide information on the signal-to-noise ratio, the fading and the appearance and decay of the propagation path. These graphs are followed by another two that show axial ratio and tilt angle, two polarization characteristics that are calculated from the measured power and phase difference.

D. Observations of the Hungarian beacon

Figs. 19 and 20 show the power and relative phase of the Es signal from HG7BVA measured in two polarization planes on 18 August 2018. This beacon transmits its identification message in Morse code using frequency shift keying (FSK), with a frequency shift of 580 Hz. To improve the signal-to-noise ratio, the FSK 'mark' and 'space' frequency components are filtered separately using narrow filters (25 Hz), after which their power is recombined. The brief down-strokes in the raw sample plot in Fig. 19 occur at the switching intervals between the mark and space, when no signal is present for a very short interval. It can be seen from Fig. 19 that the horizontally polarized component is generally 5 – 10 dB stronger than the vertical one, indicating that the polarization is highly elliptical, and that the fading patterns on both polarizations seem synchronized and very similar.

Figs. 21 and 22 show the key parameters of the polarization ellipse, calculated from the measured values shown in Figs. 19 and 20 on a per-sample basis. The axial ratio (Fig. 21) and the tilt angle (Fig. 22), which is the angle of the major axis of the ellipse to the horizontal, clearly show just over a minute of stable right-hand elliptical polarization, with an axial ratio of about 4 and a nearly constant angle to the horizontal of about 12° . Some instability is observed near the beginning and end of the recording as the Es path builds and fades, but not in the long middle section.

For a generalized combination of the ordinary and extraordinary waves, a stable right-hand elliptical polarization state for this length of time implies that the phase relationship between the two characteristic waves (and hence the relative path length travelled) is constant over an extended period. A more plausible explanation, however, would be that during this period only the extraordinary wave

was present because the Es ionization density was too low to reflect the ordinary wave. The downward extraordinary wave normally exhibits right-hand elliptical polarization in the Northern Hemisphere [2, pp 65-74], [47]. The high degree of ellipticity also seems to be consistent with magneto-ionic propagation and the QT approximation. These initial observations will be the subject of further investigation.

E. Observations of the Spanish beacon

Figs. 23 and 24 show power and relative phase for the Es signal from ED7YAD recorded on 29 July 2018. The Morse code identification message from this beacon is transmitted by on-off keying, therefore there are significant inter-symbol and inter-message cycle breaks in transmission as can be seen in Fig. 22. The moving average ignores these outages and remains accurate, so the trends can still clearly be seen.

In contrast to the Hungarian path (Fig. 19), the fading patterns for horizontal and vertical polarization are at times similar, but at other instances they differ significantly and deep fades occur in one of them while the other remains stable. The deep fades could indicate multipath or polarization fading caused by interference of the ordinary and extraordinary wave, each subject to different and variable path delays.

The polarization analysis in Figs. 25 and 26 indeed shows clear signs of polarization fading. Continuous and dramatic variations are observed in the tilt angle, axial ratio and sense of rotation of the polarization ellipse throughout the two-minute recording. For example, between 16:27:40 and 16:27:50 UTC the polarization changes from right hand circular (axial ratio near 1), to right hand elliptical, to linear (axial ratio > 100), then to left hand elliptical, to almost circular again but left hand this time, back to linear and finally to right hand elliptical again. Complete rotation of the polarization ellipse can also be seen around 16:28:15 and 16:28:30.

This is a strong indicator of magneto-ionic propagation of both the ordinary and extraordinary waves, although further work is required to confirm this. A larger volume of recordings must be analyzed before more general conclusions can be drawn.

F. Fading depth and fading frequency

The initial focus of our research has been investigating differential fading between orthogonal polarizations, which we have termed 'polarization fading'. But the technique we have described will also be effective in the investigation of common-mode fading, where the overall magnitude of a signal is changing rather than the shape and orientation of the polarization ellipse. Further work is required but some early observations can be made, based on the initial results reported here.

The recording of the Hungarian beacon (Fig. 19) shows the overall rise and fall of the signal over a two-minute period, upon which is superimposed a regular common-mode fading pattern with a period of about 5 seconds and a depth of about 4 dB. There is little differential-mode fading because the polarization state is largely stable. The recording of the Spanish beacon (Fig. 23), on the other hand, displays a great deal of differential-mode fading because of the rapidly rotating polarization ellipse. But even in this case it is possible to identify a common-mode fading pattern with a period of about 5 seconds, particularly during the constant-carrier period between 16:27:19 and 16:27:27.

These results agree well with earlier reports, including one finding that that 40% of VHF Es events lasted for less than two minutes [48], and another reporting typical fading periods of five seconds [49]. It is not possible at this stage to establish how typical this behaviour is. Full characterization of common-mode fading of Es reflections will be the subject of further research.

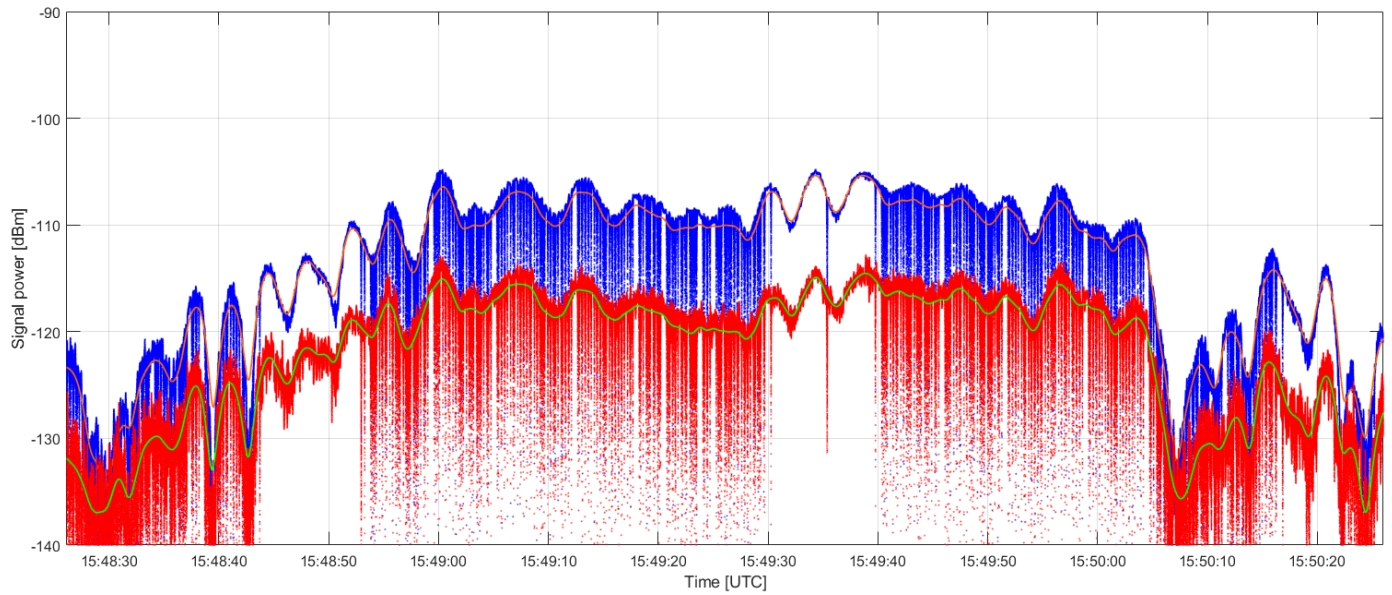


Fig. 19. Measured power vs time in two orthogonal polarization planes. Single-hop 50.430 MHz Es signal from HG7BVA in Hungary, received in the UK (1,516 km) on 18 August 2018. Blue samples/orange moving average line: horizontal polarization, red samples/green moving average line: vertical polarization.

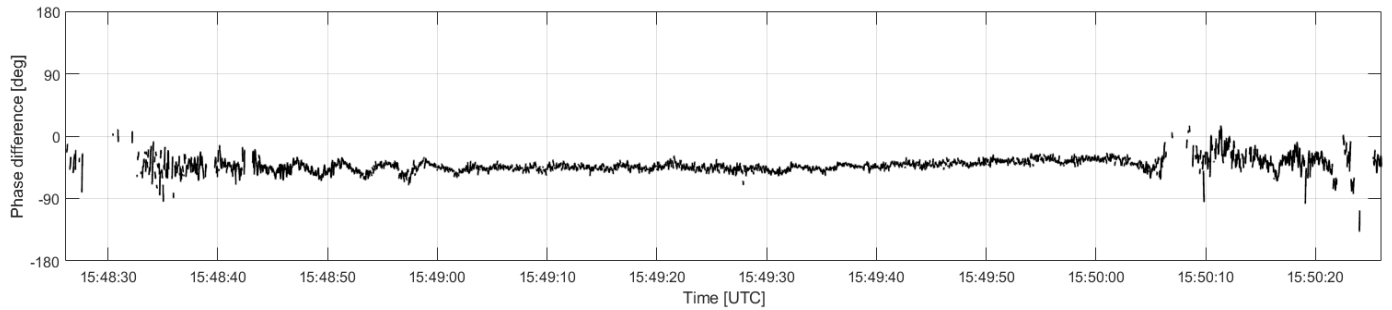


Fig. 20. Measured phase difference between two orthogonal polarization planes vs time. Single-hop Es signal from HG7BVA in Hungary, received in the UK (1,516 km) on 18 August 2018. Positive values indicate that the phase of the vertical component leads that of the horizontal component.

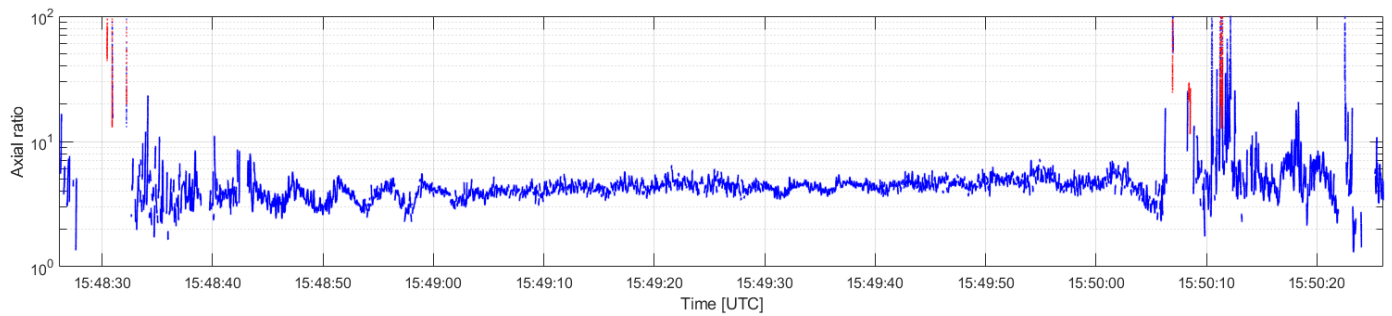


Fig. 21. Calculated axial ratio of the polarization ellipse from the measurements shown in Figs. 19 and 20. Blue: right-hand sense of rotation. Red: left-hand sense of rotation. An axial ratio of 1 represents circular polarization. A larger axial ratio signifies elliptical polarization, which approaches linear polarization as the axial ratio approaches infinity.

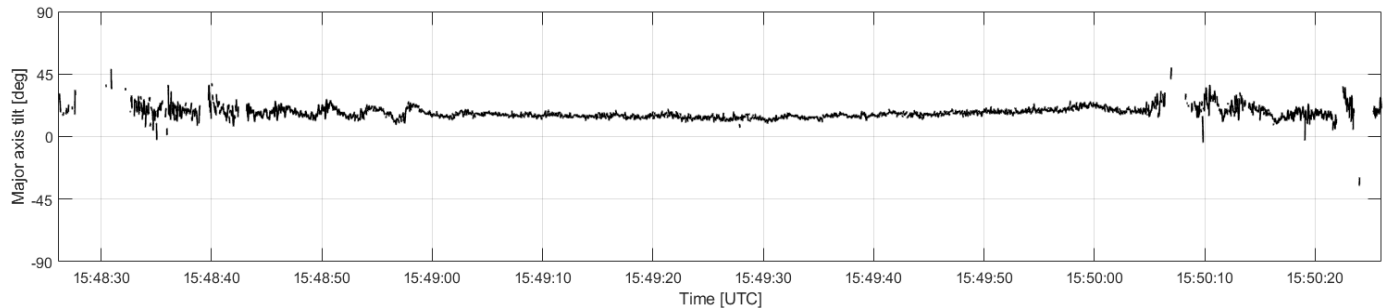


Fig. 22. Calculated tilt angle (angle of the major axis to the horizontal) of the polarization ellipse from the measurements shown in Figs. 19 and 20.

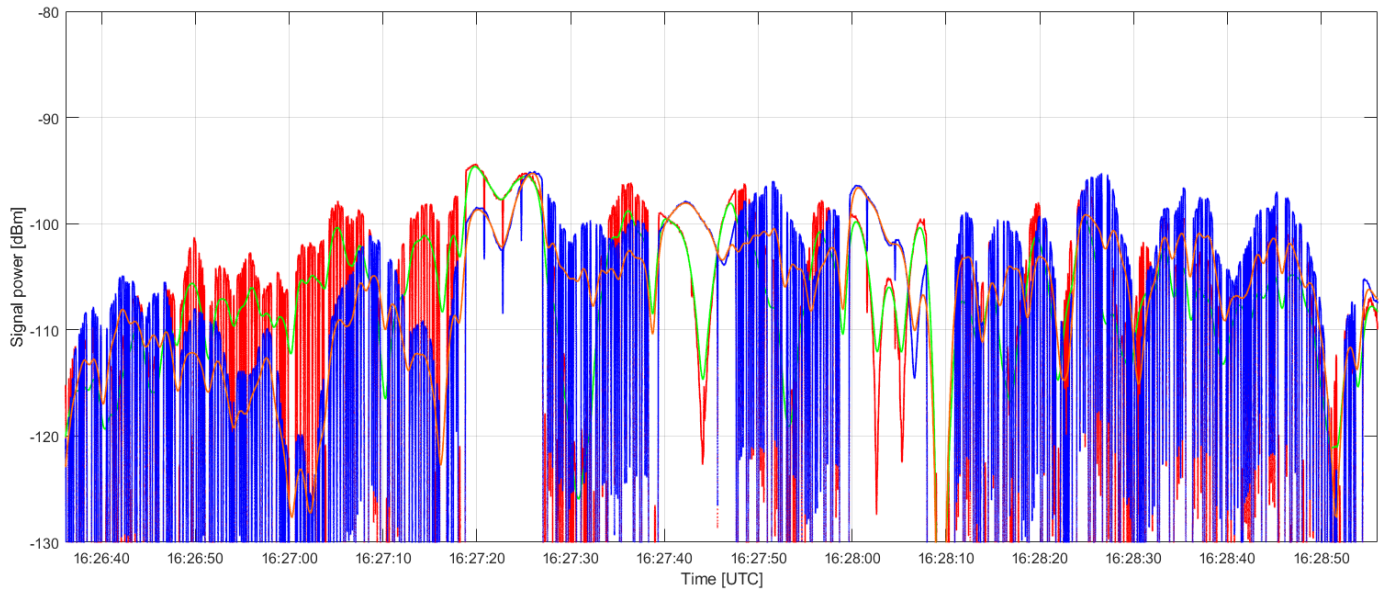


Fig. 23. Measured power vs time in two orthogonal polarization planes. Single-hop 50.475 MHz Es signal from ED7YAD in Spain, received in the UK (1,644 km) on 29 July 2018. Blue samples/orange moving average line: horizontal polarization, red samples/green moving average line: vertical polarization.

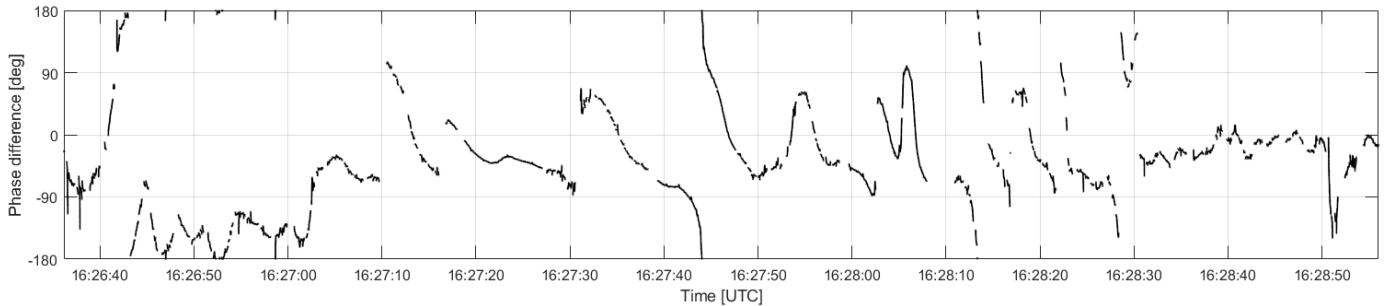


Fig. 24. Measured phase difference between two orthogonal polarization planes vs time. Single-hop Es signal from ED7YAD in Spain, received in the UK (1,644 km) on 29 July 2018. Positive values indicate that the phase of the vertical component leads that of the horizontal component.

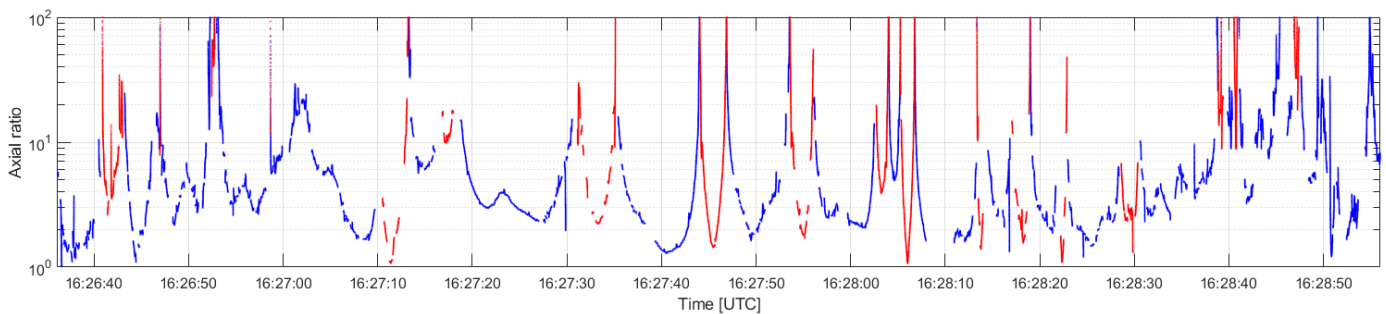


Fig. 25. Calculated axial ratio of the polarization ellipse from the measurements shown in Figs. 23 and 24. Blue: right-hand sense of rotation. Red: left-hand sense of rotation. An axial ratio of 1 represents circular polarization, which approaches linear polarization as the axial ratio approaches infinity.

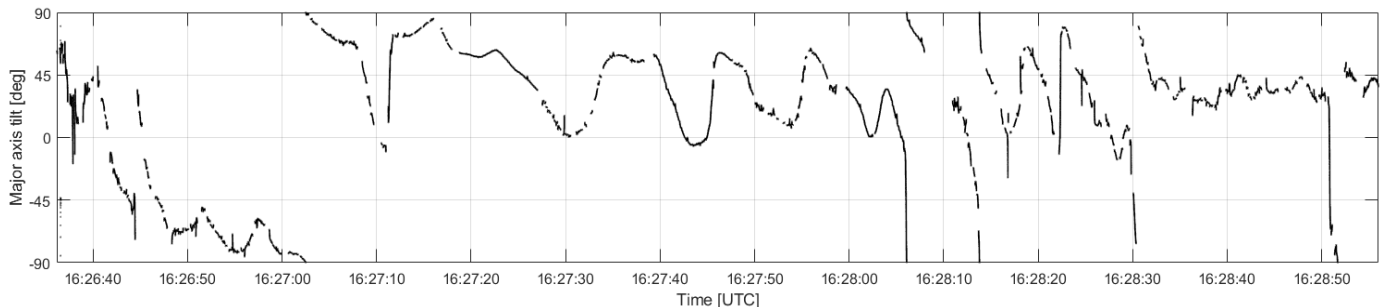


Fig. 26. Calculated tilt angle (angle of the major axis to the horizontal) of the polarization ellipse from the measurements shown in Figs. 23 and 24.

IX. CONCLUSION AND FURTHER WORK

The work here represents a rigorous analysis of a novel measurement system and some preliminary results. We have shown that significant improvements are achievable compared to instruments used in previous polarimetric Es research. Recent advances in synchronous multi-channel software-defined digital receiver platforms, and low-sidelobe VHF Yagi antennas, enable a step change in sensitivity, temporal resolution and stability. Such a system allows precise correction of system-induced and external biases during post-processing of recorded data. The instrument and its design have been described in sufficient detail to allow verification and reproduction.

In addition, we have shown that a thorough analysis of the influence of the ground reflection is essential in polarimetric measurements at low, variable elevation angles. This analysis shows that polarization cannot be measured accurately above the pseudo-Brewster angle, and that the interference pattern of the direct wave and its ground reflection impose a maximum antenna height.

Although they represent only preliminary results, we believe that the two recordings analyzed here do provide compelling evidence that Es-layer propagation at 50 MHz exhibits the characteristics of magneto-ionic double refraction. The highly elliptically polarized signal received from the Hungarian beacon and the major variations in the elliptically polarized signal received from the Spanish beacon would be difficult to explain through any other plausible mechanism.

Further work will explore the general applicability of the provisional conclusions offered here, by detailed analysis of the much larger number of Es propagation events recorded in 2018 over a wide range of azimuths and distances. These results will be combined with data from other types of measurement (e.g. ionosondes) and with the results of 3-D ray trace modelling. A more detailed exploration of the predicted magneto-ionic polarization for the QT path from Hungary will also allow a comparison of calculated polarization ellipse parameters with the observed values.

It may also be feasible to use autocorrelation techniques to separate the two characteristic waves by their different time delays, and then to measure their individual polarizations. This could provide conclusive evidence of the magneto-ionic nature of the reflection of VHF signals from Es clouds. The recorded multi-channel data will also allow detailed analysis of common-mode fading patterns and their relationship to polarization fading, which might reveal new information about the structure and movement of sporadic-E clouds.

Further work on the system design is also possible. Limitations of the current system lie (a) in the horizontal half-power beam width of the antenna of approximately 45°, limiting the azimuthal coverage of observations, and (b) the interference pattern caused by the ground reflection, which inhibits accurate high-angle (>10°) observations. The former can be overcome by using multiple antenna-receiver combinations, but at increased cost and complexity. Alternatively, stacked smaller Yagi antennas could give a wider horizontal beamwidth and a smaller vertical beamwidth, but calibration challenges might increase measurement uncertainty.

ACKNOWLEDGMENT

The authors thank the designer of the LFA Yagi antennas, Justin Johnson of InnovAntennas Ltd, for the antenna model used in our simulations and Marcus Walden for discussions on the limiting polarization in magneto-ionic propagation. The authors also thank the University of Bath, which sponsored CJD's PhD research, the UK Natural Environment Research Council for CNM's KE Fellowship, NE/P006450/1, and the Radiocommunications Agency Netherlands for the use of its FEKO antenna simulation software. All data created during this research is openly available from the University of Bath Research Data Archive.

REFERENCES

- [1] E. V. Appleton, and G. Builder, "The Ionosphere as a doubly-refracting medium," *Proc. Phys. Soc.*, 45 (2), 1933, pp. 208-220.
- [2] J. A. Ratcliffe, *The magneto-ionic theory and its applications to the ionosphere*, Cambridge University Press, 1959.
- [3] J. D. Whitehead, "Recent work on mid-latitude and equatorial sporadic-E," *J. Atmos. Terr. Phys.*, 51, 1989, pp. 401-424.
- [4] J. D. Mathews, "Sporadic E: current views and recent progress," *J. Atmos. Sol. Terr. Phys.*, 60, 1998, pp. 413-435.
- [5] C. Haldoupis, D. Pancheva, W. Singer, C. Meek, and J. MacDougall, "An explanation for the seasonal dependence of midlatitude sporadic E layers," *J. Geophys. Res.*, 112 (A06315), 2007, pp. 1-7.
- [6] V. Grassmann, "Very long distance propagation in the 144 MHz band," *Dubus*, 4, 2004.
- [7] Method for calculating sporadic-E field strength, Recommendation ITU-R P.534-5 (02/2012), Int. Telecomm. Union, Geneva, 2012.
- [8] K. Davies, *Ionospheric Radio*, Peter Peregrinus, London, 1990.
- [9] E. K. Smith, and K. Igarashi, "VHF sporadic E – a significant factor for EMI," presented at Int. Symp. on EMC, 1997, pp. 29-32.
- [10] X. Yue, *et al.*, "Characterizing GPS radio occultation loss of lock due to ionospheric weather," *Space Weather*, 14, 2016, pp. 285-299.
- [11] K. Miya, K. Shimizu, and T. Kojima, "Oblique-incidence sporadic-E propagation and its ionospheric attenuation," *Radio Sci.*, 13, 1978, pp. 559-570.
- [12] J. A. Harvey, "Movement of sporadic E ionization," *Austr. J. Phys.*, 8, 1955, pp. 523-534.
- [13] K. Rawer, "Definitions of frequency parameters of Es-layers and their accuracy," in *Ionospheric Sporadic E: International Series of Monographs on Electromagnetic Waves*, Pergamon, 1962, pp. 151-165.
- [14] W. Sun, *et al.*, "Strong Sporadic E Occurrence Detected by Ground-Based GNSS," *J. Geophys. Res.-Space*, 123, 2018, pp. 3050-3062.
- [15] E. V. Appleton and R. Naismith, "Weekly measurements of upper-atmospheric ionization," *Proc. Phys. Soc.*, 45 (389), 1933.
- [16] K. Miya, "My memory of efforts in developing CCIR Recommendation 534-3: method for calculating sporadic-E field strength," *IEEE Ant. Prop. Mag.*, 38, 1996, pp. 90-93.
- [17] C. Haldoupis, "A Tutorial Review on Sporadic E Layers," in *Aeronomy of the Earth's Atmosphere and Ionosphere*, IAGA Book Series 2, 2011, pp. 381-394.
- [18] E. K. Smith, "Temperate zone sporadic-E maps (foEs > 7 MHz)," *Radio Science*, 13 (3), 1978, pp. 571-575.
- [19] E. K. Smith, *Worldwide occurrence of sporadic E*, No. COM-75-10277; NBS-Circ-582, National Bureau of Standards, Central Radio Propagation Lab., Boulder, Colo., USA, 1957, pp. 178-183.
- [20] L. G. Smith, and E. A. Mechtly, "Rocket observations of sporadic-E layers," *Radio Sci.*, 7, 1972, pp. 367-376.
- [21] N. Christakis, C. Haldoupis, Q. Zhou, and C. Meek, "Seasonal variability and descent of mid-latitude sporadic E layers at Arecibo," *Ann. Geophys.*, 27 (3), 2009, pp. 923-931.
- [22] J. M. Grebowsky and D. Bilitza, "Sounding rocket data base of E- and D-region ion composition," *Adv. Space Res.*, 25, 2000, pp. 183-192.
- [23] W. R. From, and J. D. Whitehead, "On the peculiar shape of sporadic E clouds," *J. Atmos. Terr. Phys.*, 40 (9), 1978, pp. 1025-1028.
- [24] D. L. Hysell and J. D. Burcham, "The 30-MHz radar interferometer studies of midlatitude E region irregularities," *J. Geophys. Res.*, 105 (A6), 2000, pp. 12, 797-12, 812.
- [25] M. Yamamoto, *et al.*, "Spatial structure of the E region field-aligned irregularities revealed by the MU radar," *Radio Science*, 29 (1), 1994, pp. 337-347.
- [26] Y. U. Tong, J. D. Mathews, and W-P. Ying, "An upper E region quarterdiurnal tide at Arecibo?" *JGR: Space Physics*, 93 (A9), pp. 10047-10051.
- [27] A. Huuskonen, *et al.*, "Ion composition in sporadic E layers measured by the EISCAT UHF radar," *JGR: Space Physics*, 93 (A12), 1988, pp. 14603-14610.

- [28] W. R. From, "Sporadic E movement followed with a pencil beam high frequency radar," *Planetary and Space Science*, 31 (12), 1983, pp. 1397-1407.
- [29] I. N. Muafiry, K. Heki, and J. Maeda, "3D tomography of midlatitude sporadic-E in Japan from GNSS-TEC data," *Earth Planets and Space*, 70(45), 2018.
- [30] R. D. Egan, and A. M. Peterson. "Backscatter observations of sporadic E," in *Ionospheric Sporadic E: International Series of Monographs on Electromagnetic Waves*, Pergamon, 1962, pp. 89-109.
- [31] R. Barnes, "Analysis of Es traces from a calibrated oblique ionosonde," *J. Atmos. Terr. Phys.*, 57 (14), 1995, pp. 1753-1761.
- [32] C. Arras, *et al.*, "A global climatology of ionospheric irregularities derived from GPS radio occultation," *Geophys. Res. Letters*, 35 (L14809), 2008, pp. 1-4.
- [33] C. Arras, and J. Wickert, "Estimation of ionospheric sporadic E intensities from GPS radio occultation measurements," *J. Atmos. Terr. Phys.*, 171, 2018, pp. 60-63.
- [34] L-C. Tsai, *et al.*, "Global morphology of ionospheric sporadic E layer from the FormoSat-3/COSMIC GPS radio occultation experiment," *GPS Solutions*, 22 (4), 2018, 118.
- [35] W. J. Baggaley, "Seasonal characteristics of daytime Es occurrence in the Southern Hemisphere," *J. Atmos. Terr. Phys.*, 47 (6), 1985, pp. 611-614.
- [36] EBU Technical Centre, "Ionospheric propagation in Europe in VHF television band I," EBU Technical Document TECH 3214, Vol. I and II, European Broadcasting Union, Brussels, Belgium 1976
- [37] E. K. Smith, "Some unexplained features in the statistics for intense sporadic E (Statistical evaluation of periodic variations in intense sporadic E layer)," in *2nd Seminar on the cause and structure of temperate latitude sporadic E*, vol. 1, 1968.
- [38] J. D. Whitehead, "The formation of the sporadic-E layer in the temperate zones," *J. Atmos. Terr. Phys.*, 20 (1), 1961, pp. 49-58.
- [39] L-H. Qiu, X. Zuo, T. Yu, Y-Y. Sun, and Y. Qi, "Comparison of global morphologies of vertical ion convergence and sporadic E occurrence rate," *Adv. Space Res.*, 63 (11), 2019, pp. 3606-3611.
- [40] J. W. MacDougall, J. M. C. Plane, and P. T. Jayachandran, "Polar cap sporadic-E: Part 2, modeling," *J. Atmos. Terr. Phys.*, 62 (13), 2000, pp. 1169-1176.
- [41] J. M. C. Plane, "Atmospheric chemistry of meteoric metals," *Chem. Rev.*, 103 (12), 2003, pp. 4963-4984.
- [42] C. J. Davis, and C. G. Johnson, "Lightning-induced intensification of the ionospheric sporadic E layer," *Nature*, 435 (7043), 2005, pp. 799-801.
- [43] K. Hocke, T. Tsuda, and A. de la Torre, "A study of stratospheric GW fluctuations and sporadic E at midlatitudes with focus on possible orographic effect of Andes," *J. Geophys. Res. D: Atmos.*, 107, no. D20 (2002): ACL-5.
- [44] V. Barta, *et al.*, "Searching for effects caused by thunderstorms in midlatitude sporadic E layers," *J. Atmos. Sol. Terr. Phys.*, 161, 2017, pp. 150-159.
- [45] K. Miya and T. Sasaki, "Characteristics of ionospheric Es propagation and calculation of Es signal strength," *Radio Sci.* 1 (1), 1966, pp. 99-108.
- [46] C. S. Gillmor, "Wilhelm Altar, Edward Appleton, and the magneto-ionic theory," *Proc. Amer. Phil. Soc.*, 126 (5), 1982, pp. 395-440.
- [47] B. A. Witvliet, *et al.*, "Measuring the Isolation of the Circularly Polarized Characteristic Waves in NVIS Propagation," *IEEE Antennas Propag. Mag.*, 2015, 57 (3), pp. 120-145.
- [48] K. J. Edwards, L. Kersley, and L. F. Shrubsole, "Sporadic-E propagation at frequencies around 70 MHz," *Radio Electron. Eng.*, 54 (5), 1984, pp. 231-237.
- [49] T. S. Kerblay, G. N. Nosova, R. G. Minullin and R. A. Kurganov, "Periods of fluctuations of signals produce by ionospheric scattering and reflection from Es-layer on frequencies of 27.8 and 40.3 MHz," *Geomagn. Aeron.*, 17, 1977, pp.231-236.
- [50] R. H. Clarke and D. V. Tibble, "Measurement of the elevation angles of arrival of multicomponent HF skywaves," *Proc. Inst. Electr. Eng.*, 125 (1), 1978, pp. 17-24.
- [51] D. F. Martyn, "The propagation of medium radio waves in the ionosphere," *Proc. Phys. Soc.*, 47 (2), 1935, pp. 323-339.
- [52] G. Millington, "The relation between ionospheric transmission phenomena at oblique incidence and those at vertical incidence," *Proc. Phys. Soc.*, 50 (5), 1938, pp. 801-825.
- [53] L. F. McNamara, *The Ionosphere: Communications, Surveillance, and Direction Finding*. Krieger Publishing Company, Malabar, FL., 1991, pp. 167-168.
- [54] N. Smith, "The relation of radio sky-wave transmission to ionosphere measurements," *Proc. IRE*, 27 (5), 1939, pp. 332-347.
- [55] T. S. Kerblay, G. N. Nosova, R. G. Minullin and R. A. Kurganov, "M factor during radiowave reflection from an Es-layer on a 1050 km long path," *Geomagn. Aeron.*, 16, 1976, pp. 88-91.
- [56] H. G. Moeller, "Sweep frequency propagation on an 8,000 km transequatorial north south path," *Agard Conference Proceedings No. 173 on Radio Systems and the Ionosphere*, Athens, Greece, 1976.
- [57] S. Ganguly and S. Samanta, "Studies on the fading of the radio waves returned from the sporadic E-region of the ionosphere," *Indian J. Phys.*, 41, 1967, pp. 908-918.
- [58] L. H. Heisler and J. D. Whitehead, "Rapid variations in the sporadic-E region," *J. Atmos. Terr. Phys.*, 24, 1962, pp. 753-754.
- [59] J. F. Degregorio, J. W. Finney, K. Kildahl, and E. K. Smith, "Recent Sporadic-E Experimental Work in the United States," in *Ionospheric Sporadic E: International Series of Monographs on Electromagnetic Waves*, Pergamon, 1962, pp. 131-142.
- [60] M. Ichinose and S. Kainuma, "Polarization characteristics of VHF radio waves reflected by the Es-layer," *IEEE Trans. Broadcast.*, 42, 1996, pp. 82-87.
- [61] C. J. Deacon, B.A. Witvliet, and C. N. Mitchell, "Investigation of the polarization of 50 MHz signals via Sporadic-E reflection," *Nordic HF Conference*, 2019.
- [62] C. A. Balanis, *Antenna theory - analysis and design*, 3rd Ed., John Wiley & Sons Inc, 2005, pp. 50-52.
- [63] G. J. Burke, "Numerical electromagnetics code - NEC-4.2 method of moments, Part I: User's manual," LLNLSM-490875, Lawrence Livermore National Laboratory, Livermore, USA, 2011.
- [64] G. J. Burke, E. K. Miller, and A. J. Poggio, "The numerical electromagnetics code (NEC) - A brief history," *IEEE Antennas and Propagation Society Symposium*, Vol. 3, 2004.
- [65] J. D. Kraus, *Antennas*, 2nd edition, McGraw-Hill, 1988, pp. 716-719.
- [66] D. Brewster, L. D. F. R. S. Edin, and F. S. A. Edin, "On the laws which regulate the polarisation of light by reflexion from transparent bodies," *Phil. Trans. of the Royal Soc.*, Part I, London, 1815.
- [67] E. C. Jordan and K. G. Balmain, *Electromagnetic waves and radiating systems*, Prentice-Hall, 1950, pp. 630-633.
- [68] R. F. Potter, "Analytical determination of optical constants based on the polarized reflectance at a dielectric-conductor interface," *J. Opt. Soc. Am.*, 54 (7), 1964, pp. 904-906.
- [69] S. Y. Kim and K. Vedam, "Analytic solution of the pseudo-Brewster angle," *J. Opt. Soc. Am. A*, 3 (11), 1986, pp. 1772-1773.
- [70] A. Sommerfeld, "Über die Ausbreitung der Wellen in der drahtlosen Telegraphie," *Annalen der Physik*, 4. Folge, Band 28, 1909.
- [71] "Uncertainty of measurement — Part 3: Guide to the expression of uncertainty in measurement (GUM:1995)," *ISO/IEC GUIDE 98-3:2008*, Geneva, Switzerland, 2008.
- [72] H. Mott, *Polarization in antennas and radar*, New York, Wiley-Interscience, 1986.
- [73] W. L. Stutzman, *Polarization in electromagnetic systems*, Artech, 2018.
- [74] *IEEE Std 145-2013, IEEE Standard for Definitions of Terms for Antennas*, 2013.
- [75] *IEEE Std 149-1979, IEEE Standard Test Procedures for Antennas*, 1979.
- [76] W. F. Utlaut, "Siting Criteria for HF Communication Centers," Vol. 139, US Department of Commerce, National Bureau of Standards, 1962.
- [77] D. Bacon, "Reflection and scattering from rough surfaces," in *Propagation of radiowaves*, 2nd ed., 2003, pp. 100-101.
- [78] E. Thébaud, *et al.*, "International Geomagnetic Reference Field: The 12th generation," *Earth Planets Space*, 2015, 67 (1), pp. 67-79.